The Meteoritical Society

Meteoritics & Planetary Science 1–24 (2019)
doi: 10.1111/maps.13383

Effects of aqueous alteration on primordial noble gases and presolar SiC in the carbonaceous chondrite Tagish Lake

M. E. I. RIEBE[1,2*], H. BUSEMANN[1], C. M. O'D. ALEXANDER[2], L. R. NITTLER[2], C. D. K. HERD[3], C. MADEN[1], J. WANG[2], and R. WIELER[1]

[1]Institute of Geochemistry and Petrology, ETH Zürich, CH-8092, Zürich, Switzerland
[2]DTM, Carnegie Institution of Washington, 5241 Broad Branch Road, Washington, District of Columbia 20015, USA
[3]Department of Earth and Atmospheric Sciences, University of Alberta, Edmonton, Alberta T6G 2E3, Canada
[*]Corresponding author. E-mail: my.riebe@erdw.ethz.ch

(Received 21 December 2018; revision accepted 05 August 2019)

Abstract–Effects of aqueous alteration on primordial noble gas carriers were investigated by analyzing noble gases and determining presolar SiC abundances in insoluble organic matter (IOM) from four Tagish Lake meteorite (C2-ung.) samples that experienced different degrees of aqueous alteration. The samples contained a mixture of primordial noble gases from phase Q and presolar nanodiamonds (HL, P3), SiC (Ne-E[H]), and graphite (Ne-E[L]). The second most altered sample (11i) had a ~2–3 times higher Ne-E concentration than the other samples. The presolar SiC abundances in the samples were determined from NanoSIMS ion images and 11i had a SiC abundance twice that of the other samples. The heterogeneous distribution of SiC grains could be inherited from heterogeneous accretion or parent body alteration could have redistributed SiC grains. Closed system step etching (CSSE) was used to study noble gases in HNO_3-susceptible phases in the most and least altered samples. All Ne-E carried by presolar SiC grains in the most altered sample was released during CSSE, while only a fraction of the Ne-E was released from the least altered sample. This increased susceptibility to HNO_3 likely represents a step toward degassing. Presolar graphite appears to have been partially degassed during aqueous alteration. Differences in the $^4He/^{36}Ar$ and $^{20}Ne/^{36}Ar$ ratios in gases released during CSSE could be due to gas release from presolar nanodiamonds, with more He and Ne being released in the more aqueously altered sample. Aqueous alteration changes the properties of presolar grains so that they react similar to phase Q in the laboratory, thereby altering the perceived composition of Q.

INTRODUCTION

Chondrites are fragments of asteroids that never melted after accretion. Nevertheless, enough heat was provided from radioactive decay of short-lived radioisotopes, particularly ^{26}Al, in these bodies to alter the primary compositions (Brearley 2014; Davis and McKeegan 2014). Two main types of alteration are distinguished: thermal metamorphism and aqueous alteration. Thermal metamorphism occurred at temperatures between ~250 and 950 °C and ultimately resulted in homogenization of mineral compositions and coarsening and recrystallization of mineral grains (Keil 2000; Huss et al. 2006). Aqueous alteration occurred at lower temperatures of about 0–300 °C with water present, replacing the original anhydrous minerals with oxides, carbonates, and hydrated phases (Keil 2000; Brearley 2006). In this study, the fate of primordial noble gases and presolar SiC during aqueous alteration is investigated.

Primordial noble gases are carried by presolar nanodiamonds (the components "HL," "P3," "P6"), SiC (Ne-E[H]), and graphite (Ne-E[L]) grains and by a poorly characterized phase known as phase Q (Q-gases; Ott 2014). The primordial noble gas carriers were probably incorporated into all chondrite classes during

Table 1. Noble gas carriers and components discussed in this paper.

Carrier	Noble gas component	Alternative component names	Brief description
Phase Q	Q-gases	P1	Dominates Ar, Kr, Xe
Presolar SiC	Ne-E(H)[a]	Ne-G	~Pure ^{22}Ne
Presolar graphite	Ne-E(L)[a]	Ne-R	Pure ^{22}Ne
Presolar nanodiamonds	HL	Ne-A2	Dominates He, Ne; isotopically distinct Xe
Presolar nanodiamonds	P3		Ne component released at low temperatures during stepwise heating

[a]Ne-E(H) and Ne-E(L) are difficult to separate in the data sets discussed here and are therefore often discussed together as Ne-E.
Table modified after Ott (2014).

matrix accretion. A list of the noble gas components discussed in this paper is provided in Table 1. The effects of thermal metamorphism on the noble gas inventories in meteorites are relatively well known. The concentrations of primordial noble gases decrease with increasing thermal metamorphism and can be used to roughly estimate the petrologic type of a meteorite (e.g., Huss and Lewis 1995; Huss et al. 1996; Keil et al. 2015). Noble gases carried by presolar grains are progressively lost, beginning at low degrees of thermal metamorphism. No such gases are detected in ordinary chondrites of petrologic type higher than 3.8 (Schelhaas et al. 1990; Huss and Lewis 1995). The noble gases in phase Q, which is the main carrier of primordial Ar, Kr, and Xe in meteorites and also contains minor amounts of He and Ne, are more resistant to thermal alteration than those in presolar grains. Q-gases have, for example, been detected in H6 and EH5 chondrites (Moniot 1980; Huss et al. 1996), and even in achondrites, in particular in ureilites and lodranites (e.g., Göbel et al. 1978; Weigel et al. 1997; Busemann and Eugster 2002; Rai et al. 2003). With increasing metamorphic grade, the release temperature of noble gases in phase Q increases (Huss et al. 1996). There is also some evidence that the isotopic composition of the Q-gases changes due to retrapping of noble gases from presolar grains, which presumably were degassed during the thermal alteration (Huss et al. 1996). In addition, it has been shown that the He/Ar, Ne/Ar, and Ar/Xe and Kr/Xe ratios in phase Q decrease with increasing thermal metamorphism, reflecting a preferential loss of the light noble gases over the heavy ones (Busemann et al. 2000).

The effects of aqueous alteration on the noble gas carriers are less well understood than the effects of thermal metamorphism. Gas loss from most carriers during aqueous alteration is presumably small, as the most aqueously altered meteorites, CI, CR, and CM chondrites, contain among the highest concentrations of primordial noble gases carried by phase Q and presolar grains (Huss et al. 2003; Busemann et al. 2008). NanoSIMS isotopic mapping has also shown that SiC grains were not lost during aqueous alteration of CR chondrites (Davidson et al. 2014). However, it has been shown that the concentration of trapped ^{36}Ar decreases with increasing aqueous alteration in bulk CM chondrites (Browning et al. 1996; Marrocchi et al. 2014), indicating that as with thermal metamorphism, aqueous alteration results in loss of noble gases. In addition, as for thermal alteration, it has been suggested that aqueous alteration of phase Q in meteorites results in a lowering of the $(Ar/Xe)_Q$ and $(Kr/Xe)_Q$ ratios (Busemann et al. 2000). Confusingly, the $(He/Ar)_Q$ and $(Ne/Ar)_Q$ ratios are highest in the most aqueously altered CM meteorites (Busemann et al. 2000).

In this work, we investigate the effects of aqueous alteration on primordial noble gas carriers in more detail. A unique sample set that is particularly suitable for this kind of study became available with the fall of the Tagish Lake meteorite (C2-ung.) in 2000 (Brown et al. 2000). Tagish Lake fell on a frozen lake and the samples in this study were collected from the ice, only a few days after the fall and kept frozen until processed in the laboratory, thus minimizing the effects of terrestrial alteration (Herd et al. 2011). Tagish Lake contains clasts that experienced different degrees of aqueous alteration, providing a unique opportunity to study the effects of aqueous alteration within the same meteorite (Zolensky et al. 2002; Herd et al. 2011; Blinova et al. 2014a, 2014b). Herd et al. (2011) and Alexander et al. (2014) found that the four Tagish Lake samples they analyzed had very variable δD and H/C ratios in the organic matter (Table 2). The least altered sample based on petrology, 5b, had the highest δD and H/C. The sample with the lowest δD and H/C, 11v, is a collection of fragments from the ice and contains pieces with petrologic characteristics of all three other samples (Blinova et al. 2014a, 2014b). Here, we investigate if the primordial noble gases and their carriers also were affected by aqueous alteration on the Tagish Lake parent body.

Table 2. The samples analyzed in this study

Sample	5b	11h	11i	11v
Alteration[a]	Least	intermediate	intermediate	most
H/C[a]	0.72	0.594	0.51	0.44
δD (‰)[a]	1844	1470	992	815
IOM yield (wt%)[b]	1.58 ± 0.39	1.86	1.82 ± 0.05	1.77 ± 0.14
IOM sample masses (mg)				
CSSE	3.6			4.3
Stepwise pyrolysis unoxidized	0.77	0.89	0.81	0.89
Stepwise pyrolysis oxidized[c]	1.60			0.76

[a]Herd et al. (2011).
[b]Alexander et al. (2014).
[c]Residue from CSSE.

MATERIALS AND METHODS

We studied noble gases and presolar SiC grains in Tagish Lake insoluble organic matter (IOM). IOM makes up ~1.8 wt% of the Tagish Lake meteorite and was extracted from the meteorite using a CsF/HF technique (for details, see Alexander et al. 2007, 2014). For sample masses and other details about the samples, see Table 2. In addition to macromolecular organic matter, the IOM residues contain refractory presolar grains such as SiC, graphite, and nanodiamonds as well as the unidentified carrier of the Q-gases. This type of sample is also sometimes referred to as "acid-resistant residue" or "HF-HCl resistant residue." We used the same IOM sample set as the Herd et al. (2011) and the Alexander et al. (2014) studies: samples 5b, 11h, 11i, and 11v (Table 2). In IOM, primordial noble gases are concentrated compared to in bulk meteorite material and potential contamination from cosmogenic, radiogenic, and solar wind noble gases is significantly reduced as these gases mainly reside in the silicates, which are destroyed during the IOM extraction.

Two different techniques were used to analyze the noble gases, closed system step etching (CSSE, e.g., Riebe et al. [2017a] and references therein) and stepwise pyrolysis. For an overview of the analytical protocol, see Fig. 1. IOM from all four samples was analyzed using stepwise pyrolysis to compare the concentrations and compositions of primordial noble gases between the samples. IOM from all four samples was also mapped by NanoSIMS to determine the abundances of presolar SiC grains, following the method of Davidson et al. (2014). In addition, samples 5b and 11v with the highest and lowest δD values and H/C ratios, respectively, were analyzed by the much more time-consuming CSSE technique, using HNO_3 as an etching agent. We chose 11v for the CSSE analysis based on its δD and H/C ratios as these are likely the most relevant indicators of degree of alteration of the IOM, although 11i is the most altered sample on petrological grounds alone (Blinova et al. 2014a, 2014b). CSSE is a well-established technique in the noble gas laboratory at ETH Zurich to study the noble gases in phase Q (Wieler et al. 1991, 1992; Busemann et al. 2000). With this technique, phase Q is analyzed according to the original definition given by Lewis et al. (1975) in which phase Q survives IOM extraction but releases Q-gases upon oxidation, for example with HNO_3. It has been noted in previous studies that the isotopically anomalous Ne-E components carried by presolar graphite and SiC are sometimes released together with Q-gases (Wieler et al. 1992; Busemann et al. 2000). The IOM samples were recovered after the CSSE analyses (hereafter "oxidized IOM") and analyzed by stepwise pyrolysis. Most of the Q-gases were released during the CSSE experiments, facilitating the detection of other primordial noble gas components associated with presolar grains in the oxidized IOM samples.

Stepwise Pyrolysis

Unoxidized IOM separates of all four samples were analyzed using stepwise pyrolysis at 600, 1000, 1200, and 1750 °C. The oxidized 5b and 11v IOM samples after CSSE analysis were also analyzed in this way, with an additional step at ~300 °C. A re-extraction step at slightly higher temperature than the 1750 °C step released gas amounts similar to the blank for all samples. Details about the noble gas measurement protocols that are not found below can be found in Riebe et al. (2017b).

Stepwise pyrolysis blanks were measured before every sample. All six blanks were similar and hence averaged for each temperature step. The standard deviation of the blanks was used as the uncertainty of the blank correction. The blank corrections generally contribute to the uncertainties in the isotopic ratios of a few percent for some minor steps, but do not pose a problem for the major gas releasing temperature steps. The blank correction on ^{40}Ar was, as is expected for samples of IOM, high in most steps, and in some steps, no ^{40}Ar above blank level was detected. The steps for which ^{40}Ar is reported have blank corrections of up to 40%, resulting in uncertain $^{40}Ar/^{36}Ar$ ratios. Possible interferences from CO_2^{++}, $^{40}Ar^{++}$, and $H_2{}^{18}O^{+}$ on masses 20 and 22 were corrected for by the blank correction in most steps. However, corrections of up to a few percent were necessary for interferences on ^{20}Ne and ^{22}Ne in the stepwise heating of the unoxidized

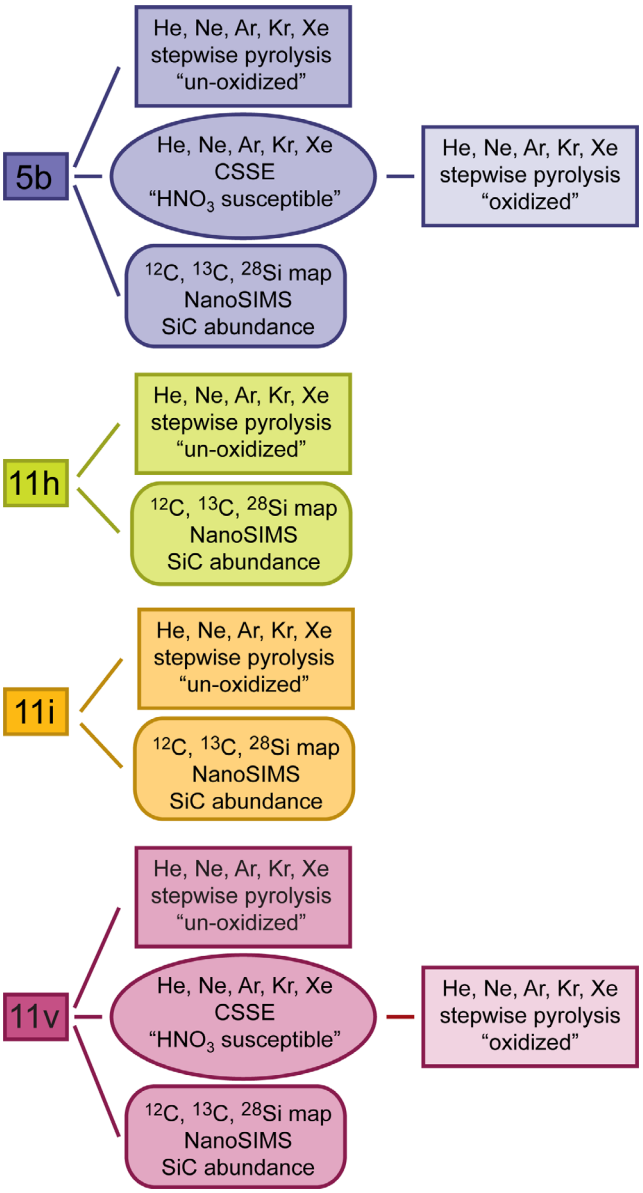

Fig. 1. Schematic overview over the Tagish Lake IOM samples analyzed in this study. Color image available in the digital version.

residues of 11v and 5b, where the interference intensities in blanks and samples were not comparable.

The high concentration of reactive gases in these samples caused problems during the separation of Ar from Kr and Xe. In some steps, more Ar was measured in the Kr and Xe separate than in the Ar separate. There are two potential explanations for this. (1) IOM residues contain a lot of hydrocarbons and it is possible that the reactive species were preferentially frozen onto the coal in the liquid nitrogen trap used for the separation, thereby inhibiting Ar from freezing onto it as well. (2) Most of the ions recorded at mass 40 in the Kr and Xe separates were not actually Ar but hydrocarbons. Based on the signal changes in the mass spectrometer during the analyses and the measured elemental ratios, we consider possibility 2 more likely. However, as we cannot fully exclude possibility 1, the reported uncertainties of Ar concentrations are the difference between the concentration of Ar corrected for "losses" in the Kr and Xe separates and without any correction for Ar losses for all steps.

The uncertainties in absolute gas concentrations for both stepwise pyrolysis and stepwise etching analyses include the statistical uncertainties (1σ), the uncertainties from blank correction, the sensitivities of the mass spectrometer, and the uncertainties of the sample masses. The uncertainties on isotopic ratios include statistical uncertainties (1σ), uncertainty of blank correction, and of the instrumental mass fractionation.

Closed System Step Etching

The CSSE technique differs from conventional noble gas extraction techniques in that the gas is extracted by etching with an acid in a high-vacuum system at low temperatures, hence avoiding simultaneous release of gas components by diffusion. CSSE is an ideal technique for analyzing phase Q as we can target the HNO_3-susceptible phases exclusively (cf. Lewis et al. 1975). All parts of the line that are in direct contact with the acid are made of Au or Pt. Two Au containers, one containing the acid and one containing the sample, are separated by a valve and connected to the gas-cleaning line and mass spectrometer. After loading and evacuation, the samples were heated to 80 °C in vacuum for about 24 h to reduce adsorbed atmospheric noble gases. The amounts of atmospheric gases still released from the sample after this heating were tested by keeping the sample volume closed for a few hours and analyzing the released gases. Compared to a so-called "procedure blank," that is, a blank of the line excluding the sample volume, the blanks of the samples prior to etching were not elevated. Atmospheric gases in the freshly loaded acid were removed by heating and cooling the acid in several steps and pumping off the released gases through a separate line bypassing the sample while the acid was kept cold. The efficiency of the degassing was tested by "acid blanks," during which the acid was left at room temperature for 15–20 min and then cooled to −50 °C for 2 h, simulating conditions during the first etch step. In the 5b etch run, the last acid blank was comparable to procedure blanks. However, the initial acid blank of atmospheric composition was higher in the 11v etch run

for the heavier noble gases (×10 Xe, ×5 Kr, ×2 Ar), which also resulted in higher contamination in the first etch steps of this sample.

Both etch runs consisted of 19 steps each, and the same sequence of etching conditions was used for the respective steps for each run (see Table 3), facilitating direct comparison. Noble gases were released by using 2 mL of 65% HNO_3 as etching agent. In the beginning of the etch runs, the samples were etched in acid vapor at room temperature for increasing times (Table 3). At step 8 (marked as "acid distillation" in Table 3), the acid was transferred to the sample volume by heating the acid to ~90 °C and cooling the sample to ~−60 °C while keeping the valve between the two containers open for ~2 h. No significant new etching occurred in this step, which is, therefore, not included in the data discussion. After the acid was transferred, the etching conditions were successively harshened by increasing etching times and temperatures, see Table 3.

The gas released in an etch step was expanded into the gas cleaning line through a Au U-trap kept at −50/60 °C to freeze out acid that might still be in the gas phase. The gas was then exposed to a series of getters to remove interfering gas species, one getter consists of CaO powder, three getters consist of commercial Zr-V-Fe pellets (ST 707 SAES™) operated at 280 °C, and three Zr-V-Fe cartridge getters were employed (SAES™ GP-50 with ST 172 getter material), operated at different temperatures. Except for the gettering and the gas extraction, the measurement protocol was very similar to the stepwise heating.

Procedure blanks were measured regularly, 16 blanks in the 11v etch run and 11 in the 5b etch run, which had a more constant blank level. For both etch runs, blanks relevant for each etch step (between 3 and 10 blanks) were averaged and the standard deviation adopted as the uncertainty of the blank level. For most etch steps and isotopes, the blank correction was <1%. Exceptions are ^{22}Ne with typical blank corrections of 2–10% and ^{40}Ar with blank corrections of typically a few % in 11v and ~15% in 5b. With the exception of some gas-poor etch steps, blank corrections resulted in less than 1% additional uncertainties in the isotopic ratios in all elements. During the 11v analysis, there was a sudden increase in the blank due to an accident in the purification line, unrelated to the etch experiment. This blank issue mainly affected the Kr and Xe measurements of steps 5–9, resulting in large uncertainties in the Kr and Xe data and no detection of Kr above the blank level in

Table 3. Concentration and isotopic composition of Ne in CSSE analyses of samples 5b and 11v. Analyses with uncertainties >100% not reported.

		5b			11v		
Step	Conditions	^{22}Ne[a]	$^{20}Ne/^{22}Ne$	$^{21}Ne/^{22}Ne$	^{22}Ne[a]	$^{20}Ne/^{22}Ne$	$^{21}Ne/^{22}Ne$
1	15 min vapor	0.07 ± 0.02	7.51 ± 1.57	0.0220 ± 0.0060	N/D	N/D	N/D
2	2 h 15 min vapor	0.12 ± 0.01	9.95 ± 1.15	0.0308 ± 0.0046	0.09 ± 0.03	11.51 ± 3.98	0.0471 ± 0.0165
3	15 h vapor	0.53 ± 0.03	9.75 ± 0.29	0.0339 ± 0.0016	0.44 ± 0.03	9.90 ± 0.72	0.0370 ± 0.0029
4	24 h vapor	0.64 ± 0.03	9.70 ± 0.24	0.0275 ± 0.0014	1.14 ± 0.04	5.32 ± 0.15	0.0178 ± 0.0009
5	65 h vapor	0.80 ± 0.04	9.74 ± 0.20	0.0293 ± 0.0011	2.22 ± 0.06	4.91 ± 0.07	0.0159 ± 0.0004
6	Mini distill[b]	0.04 ± 0.01	6.14 ± 1.35	0.0221 ± 0.0109	0.09 ± 0.03	7.83 ± 2.69	0.0246 ± 0.0090
7	288 h vapor	1.57 ± 0.06	9.41 ± 0.11	0.0267 ± 0.0007	5.18 ± 0.13	4.93 ± 0.04	0.0155 ± 0.0002
8	Acid distill[b]	N/D	N/D	N/D	N/D	N/D	N/D
9	2 h liquid RT	0.13 ± 0.02	9.36 ± 1.07	0.0286 ± 0.0036	N/D	N/D	N/D
10	24 h liquid RT	0.07 ± 0.02	10.60 ± 2.20	0.0128 ± 0.0054	0.55 ± 0.01	6.74 ± 0.07	0.0207 ± 0.0008
11	15 h liquid 35 °C	0.35 ± 0.02	10.16 ± 0.45	0.0281 ± 0.0016	0.52 ± 0.01	7.28 ± 0.07	0.0213 ± 0.0008
12	15 h liquid 45 °C	0.32 ± 0.02	9.96 ± 0.51	0.0272 ± 0.0030	1.15 ± 0.03	7.47 ± 0.04	0.0226 ± 0.0006
13	19 h liquid 55 °C	0.16 ± 0.02	10.20 ± 0.93	0.0267 ± 0.0045	1.54 ± 0.04	7.73 ± 0.04	0.0233 ± 0.0005
14	15 h liquid 65 °C	0.55 ± 0.03	9.49 ± 0.27	0.0270 ± 0.0010	3.21 ± 0.08	7.94 ± 0.03	0.0233 ± 0.0004
15	15 h liquid 75 °C	4.61 ± 0.18	8.70 ± 0.05	0.0246 ± 0.0003	1.90 ± 0.04	7.61 ± 0.04	0.0237 ± 0.0004
16	14 h liquid 85 °C	2.71 ± 0.11	7.62 ± 0.07	0.0230 ± 0.0004	1.52 ± 0.04	7.76 ± 0.04	0.0238 ± 0.0004
17	14h liquid 95 °C	1.05 ± 0.04	6.73 ± 0.11	0.0210 ± 0.0006	2.67 ± 0.06	7.85 ± 0.04	0.0252 ± 0.0004
18	66 h liquid 95 °C	2.91 ± 0.12	6.08 ± 0.04	0.0195 ± 0.0003	0.83 ± 0.02	8.10 ± 0.08	0.0286 ± 0.0009
19	76 h liquid 95 °C	0.96 ± 0.04	5.86 ± 0.10	0.0205 ± 0.0007	0.59 ± 0.01	8.35 ± 0.08	0.0294 ± 0.0011
Total		17.58 ± 0.27	8.11 ± 0.15	0.0241 ± 0.0005	23.63 ± 0.20	6.82 ± 0.08	0.0215 ± 0.0003

The tubing above the same holder was heated to 15 °C higher than the sample during heating above RT.

[a]Concentrations are given in 10^{-8} cm^3STP/g and calculated as cm^3STP/g of the total mass IOM loaded in the CSSE line.

[b]Mini distill : Sample kept at −25 °C and acid at RT for 30 min to transfer some acid to the sample volume. After this, the sample was brought up to RT for 1.5 h. Acid distill: sample kept at −60 °C and acid heated to 90 °C for 2 h.

RT = room temperature, N/D = not detected.

the gas poor step 6. Interferences from CO_2^{++}, $^{40}Ar^{++}$, and $H_2{}^{18}O^+$ at masses 20 and 22 were mostly small and corrected for by the blank subtraction in all etch steps in 11v and most etch steps in 5b. The following etch steps in 5b required additional interference corrections: step 2 (12% on ^{22}Ne), step 6 (11% on ^{20}Ne, 46% on ^{22}Ne), step 7 (3% on ^{20}Ne), and step 13 (2% on ^{20}Ne), because the $^{40}Ar^+$ and/or CO_2^+ signals in these steps were not comparable to the respective blank signals.

Argon, Kr, and Xe in step 15 in the 5b etch run could not be measured due to a too high background of hydrocarbons. The amounts of these gases in this step are estimated based on the measurements of ^{4}He and ^{20}Ne in step 15 and assuming the same Ar-Xe ratios relative to ^{4}He and ^{20}Ne as in averaged steps 14 and 16. For some steps, the ^{78}Kr/^{84}Kr and ^{80}Kr/^{84}Kr ratios deviate to an unreasonable degree from the values for Q and air. This is most likely due to the presence of residual hydrocarbons on masses 78 and 80. Because the ^{78}Kr and ^{80}Kr isotopes are of little interest in this study, they are not reported.

NanoSIMS

Unoxidized IOM samples from all four lithologies were isotopically mapped in the NanoSIMS to determine the abundances of SiC grains independently from noble gases, following the method of Davidson et al. (2014). A micromanipulator was used to transfer ~15–40 μm fragments of IOM to clean, annealed gold foils mounted onto aluminum for good charge transfer. The IOM was subsequently pressed into the gold. The Cameca NanoSIMS 50L ion microprobe at the Carnegie Institution was used to collect ion images of the samples. A ~1 pA focused Cs^+ primary ion beam was scanned across the sample with raster sizes of 20 × 20 μm, 512 × 512 pixels. For each area, 12 frames, that is, repeats of each image, were collected with a dwell time of 1.5 ms per 39 × 39 nm pixel, resulting in a total acquisition time of each map of 1 h 26 min. The effective spatial resolution was <130 nm. The fragments were simultaneously mapped for negative secondary ions of ^{16}O, ^{17}O, $^{12}C^{12}C$, $^{13}C^{12}C$, $^{12}C^{14}N$, $^{12}C^{15}N$, and ^{28}Si, and secondary electrons. The instrument was tuned to provide sufficient mass resolution to separate molecular interferences such as $^{16}O^1H$ on ^{17}O, $^{13}C^{14}N$ on $^{12}C^{15}N$, and $^{12}C_2{}^1H$ on $^{13}C^{12}C$ (M/ΔM ~5600). Prior to analysis, the samples were pre-sputtered over an area of 25 × 25 μm with a more intense primary beam for ~7 min to remove surface contamination and to implant Cs.

The images were analyzed using the L'IMAGE software (L. R. Nittler, Carnegie Institution, http://limagesoftware.net). The images were corrected for the 44 ns dead time of the electron multiplier counting system and individual frames were spatially aligned to correct for small drifts during the acquisition time. Following Davidson et al. (2014), presolar SiC grains were identified if they had a $^{13}C/^{12}C$ at least 3σ away from the average ratio of the IOM fragment and a measured $^{28}Si/^{12}C$ at least three times higher than the average (Fig. 2). An effect of this definition is that grains with $^{12}C/^{13}C$ ratios between 80 and 100 are effectively undetectable (Fig. S1 in supporting information). Other uncertainties and potential biases of this method are discussed in detail in Davidson et al. (2014). Each image was carefully assessed so that anomalous C on the edge of a Si-rich area was not misinterpreted as a SiC grain (Fig. S2 in supporting information) and anomalies in areas smaller than 130 nm in diameter were not included. The outline of each SiC grain was defined as the area fulfilling the two criteria above; $^{12}C/^{13}C$ ratios and grain diameter were determined from

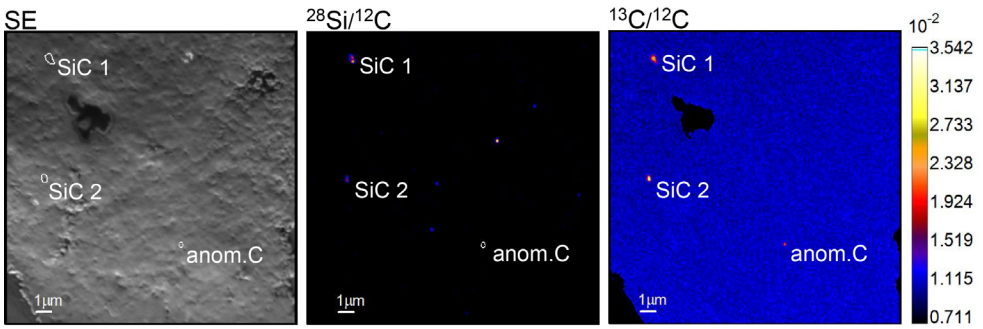

Fig. 2. NanoSIMS images illustrating the distinction between presolar SiC and isotopically anomalous carbon. The first panel is a secondary electron image in which the three areas of interest are marked. In the second panel, the Si/C ratio map is shown—the two SiC grains have higher Si/C ratios than most of the surrounding IOM. The outline of the anomalous C is marked in the second panel; in this region of interest, the Si/C ratio is not elevated compared to the rest of the particle. In the last panel, the carbon isotopic map is shown; the two SiC grains and the area of anomalous C have clearly elevated $^{13}C/^{12}C$ ratios compared to the bulk of the particle. Color image available in the digital version.

Table 4. Presolar SiC NanoSIMS data.

Sample	Mapped area (μm^2)	Number of SiC grains	SiC abun. mx-norm. (ppm)		Diameter (nm)				$^{12}C/^{13}C$
			NanoSIMS[a]	Ne-E[b]	Ave.[c]	Max	Min	Ave. corr[d]	Ave.[c]
5b	7865	19	10 ± 5	11	283 ± 199	1002	139	244	61 ± 12
11h	6724	28	14 +3/−4	13	265 ± 98	583	132	231	72 ± 10
11i	6454	51	25 ± 4	33	257 ± 107	566	132	220	69 ± 12
11v	5908	18	12 ± 4	9	293 ± 130	596	139	260	64 ± 8

[a]Uncertainties (1σ) estimated based on Monte Carlo simulation, see the NanoSIMS section.
[b]SiC abundance estimated from the concentration of Ne-E released ≥1000 °C using 0.000165 cm^3 Ne-E/g SiC from Lewis et al. (1994) and Huss and Lewis (1995).
[c]Uncertainty is standard deviation.
[d]Following correction for NanoSIMS beam broadening as described in Nittler et al. (2018).

the pixels within this area. Carbon isotopic compositions of the bulk IOM samples given by Alexander et al. (2014) were used to correct for instrumental mass fractionation. The diameters of the SiC grains are given as uncorrected and corrected values in Table 4. The apparent size of a presolar SiC grain in the ion images depends on the actual size of the grain and the size of the primary ion beam. For the corrected sizes, an assumed 120 nm beam diameter has been subtracted in quadrature from the original diameter following Nittler et al. (2018).

The concentration of SiC was calculated based on the area of SiC compared to the total area analyzed following Davidson et al. (2014). The mass fractions of the IOM in the lithologies (1.58–1.86 wt%; Alexander et al. 2014) as well as the density difference between SiC and IOM were also taken into account (see Davidson et al. 2014). The matrix abundance was assumed to be identical in the different samples based on the samples having very similar abundances of IOM C (Alexander et al. 2014) and was set to 75%. Since we are mainly interested in comparing the abundance of SiC between the different Tagish Lake samples, the absolute matrix abundance is not that important. Caution should be taken when comparing the SiC abundances reported here to those in the literature as the value of 75% matrix abundance for Tagish Lake used here is somewhat arbitrary. Uncertainties in the abundance estimates are statistical and estimated with the Monte Carlo method described by Nittler et al. (2018).

RESULTS

Summary of Results

Most of the heavy noble gases were released from the IOM during the CSSE experiments, between ~70–75% of ^{36}Ar and ~80–85% of ^{84}Kr and ^{132}Xe, whereas most of the He and Ne remained in the residue during etching (~20% of the ^4He was released and ~35% of the ^{20}Ne). These results were expected and reflect that most of the ^4He and ^{20}Ne are carried by presolar nanodiamonds that retain their gases during HNO_3 treatment, whereas most of the heavy noble gases are carried by the oxidizable phase Q that released most of its noble gases during etching with HNO_3 in the CSSE experiment.

Similarities Between the Different Tagish Lake Samples

1. The samples contain, as expected, noble gases that are best understood as mixtures of the primordial noble gas components Q (phase Q), HL (presolar nanodiamonds), Ne-E (presolar graphite and SiC), possibly P3 (presolar nanodiamonds), and minor amounts of cosmogenic ^3He (Figs. 3–5, S3 in supporting information).
2. There are only minor differences in the concentrations of Q, HL, and P3 components between the samples (Fig. S4 in supporting information).
3. In both CSSE analyses (5b and 11v), the late etch steps released gas with higher $^4He/^{36}Ar$ and $^{20}Ne/^{36}Ar$ ratios, but lower $^4He/^{20}Ne$ ratios than the early and intermediate etch steps, indicating gas release from an additional phase in the late etch steps (Fig. 6). During stepwise heating, the 1200 °C steps in both the unoxidized and oxidized IOM of all samples also released gases with low $^4He/^{20}Ne$ ratios that were possibly retained in the same phase(s) as the gases released in the late etch steps (Fig. 4; Table 5).
4. The sizes (Fig. S5 in supporting information) and $^{12}C/^{13}C$ ratio (Fig. S1) distributions of presolar SiC grains, as determined by NanoSIMS, are similar in all the samples, and the concentrations are similar in the 5b, 11h, and 11v samples.

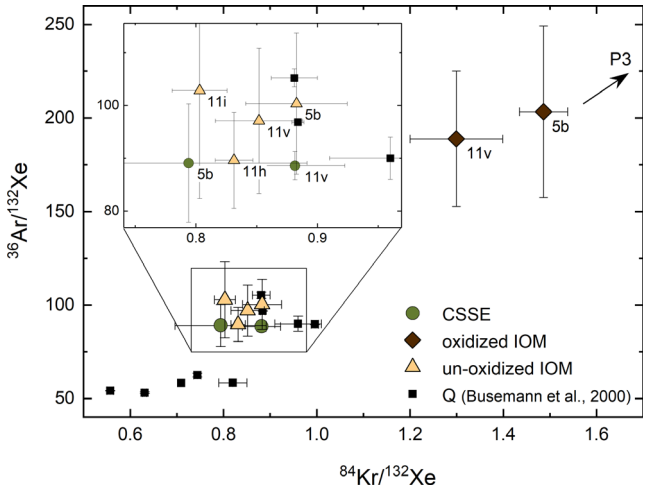

Fig. 3. Heavy noble gas elemental ratio plot. There is no significant difference in the heavy elemental composition of the unoxidized IOM samples (light triangles). In addition, there is no resolvable difference of Ar/Xe and Kr/Xe ratios between the HNO_3 susceptible gases released in the CSSE experiment (green circles; mainly Q gases) and these ratios in the unoxidized residues, indicating that the heavy noble gases in the IOM are as expected dominated by Q-gases. The oxidized IOM (dark diamonds) remaining after the CSSE experiments has higher Ar/Xe and Kr/Xe ratios than the other samples, showing that the trapped gases residing in presolar grains have higher Ar/Xe and Kr/Xe ratios than Q. The ratios plotted here have been corrected for atmospheric contamination. For ^{36}Ar, this correction is based on the assumption that all ^{40}Ar is of atmospheric origin; for Xe, it is based on mixing between Q (Busemann et al. 2000) and air (Basford et al. 1973) using $^{128}Xe/^{132}Xe$ and $^{136}Xe/^{132}Xe$, and for Kr assuming the percentage of atmospheric Kr to be the same as that of atmospheric Xe. Color image available in the digital version.

Differences Between the Different Tagish Lake Samples

1. The concentrations of Ne-E (carried by presolar SiC and graphite) in the unoxidized IOM samples are highly variable, differing by a factor of 3.7 between the highest and lowest concentrations (Fig. 7). This puzzling fact was investigated further by determining the abundances of presolar SiC grains in the IOM samples by NanoSIMS mapping. The NanoSIMS investigation showed that presolar SiC grains are heterogeneously distributed between the samples following the same pattern as the Ne-E data and, hence, indicate that the carrier of the heterogeneously distributed Ne-E is SiC. The abundance of SiC determined by NanoSIMS is about twice as high in the second most altered sample 11i as in the other samples (Fig. 8).
2. Ne-E was almost completely released in the CSSE analysis of the more altered sample 11v, that is, essentially all Ne-E gases from both presolar graphite and SiC were released. Only ~35% of the Ne-E in the less altered sample 5b was released in during CSSE analysis (Fig. 7).
3. The CSSE analysis showed that Tagish Lake 11v has the highest $^{20}Ne/^{36}Ar$ and $^{4}He/^{36}Ar$ ratios measured in the HNO_3 susceptible portion of IOM so far, whereas the gases released from 5b have lower ratios (Fig. 9). This is in agreement with previous observations that the $^{20}Ne/^{36}Ar$ and $^{4}He/^{36}Ar$ ratios of phase Q are higher in more aqueously altered samples than in less altered samples (Busemann et al. 2000).

Stepwise Pyrolysis of Unoxidized IOM

The noble gases in the unoxidized IOM samples are a mixture of primordial noble gases hosted in phase Q and presolar grains. Most of the heavy noble gases (Ar, Kr, Xe) are Q-gases. The $^{36}Ar/^{132}Xe$ and $^{84}Kr/^{132}Xe$ ratios (Fig. 3) and the isotopic ratios of Ar, Kr, and Xe are similar to those previously determined for the Q component (Busemann et al. 2000; Tables 6, 7, S5, S6 in supporting information).

The light noble gases (He, Ne) were as expected predominantly released from presolar grains. This is seen in Fig. 4: the $^{4}He/^{132}Xe$ and $^{20}Ne/^{132}Xe$ ratios are significantly higher than those of the Q component, consistent with gas release from presolar grains with higher $^{4}He/^{132}Xe$ and $^{20}Ne/^{132}Xe$ ratios than Q. The Ne three isotope plot (Figs. 5a and 5b) shows that the Ne in all samples is in agreement with a mixture of gases from presolar nanodiamonds (HL, P3), presolar graphite, and SiC (Ne-E). The total Ne released in each sample plots on what appears to be a mixing line between Ne-E and a point between HL and P3. This indicates that the mixture of HL and P3 in nanodiamonds (and possible Q) is rather constant between the different samples, whereas the relative concentration of Ne-E from presolar SiC and graphite is variable. This is supported by the fact that the concentrations of ^{4}He, ^{20}Ne, ^{36}Ar, ^{84}Kr, and ^{132}Xe are similar in all samples (Fig. S4), indicating similar concentrations of Q and presolar nanodiamonds in all samples. However, as seen in Table 8 and Fig. 7, the concentrations of Ne-E are highly variable (Ne-E deconvolution described in Data S1 in supporting information). The concentrations of Ne-E in the Tagish Lake samples of 1.2–4.3 $\times$ 10^{-9} cm^3STP/g meteorite are comparable to those previously determined for CI and CM2 chondrites of 1.5–6.4 $\times$ 10^{-9} cm^3STP/g (Huss and Lewis 1995; Huss et al. 2003), but lower than those in two Tagish Lake samples that were determined by Nakamura et al. (2003) to be 7–8 $\times$ 10^{-9} cm^3STP/g.

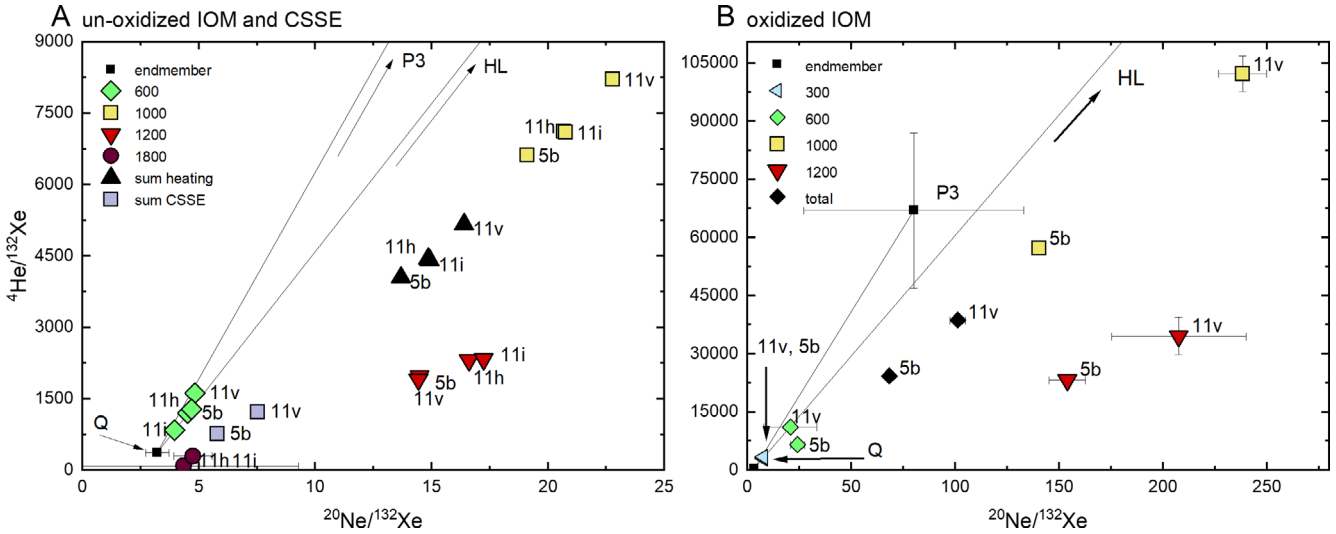

Fig. 4. $^4He/^{132}Xe$ and $^{20}Ne/^{132}Xe$ ratios. A) The ratios of the gases released in stepwise heating of the unoxidized IOM and the composition of the sum of the gases released during CSSE of 5b and 11v. B) The gases released during stepwise heating of the oxidized IOM. Note that the scales are different in the two panels. Color image available in the digital version.

Looking only at samples 5b, 11h, and 11v in Fig. 7, the concentration of Ne-E appears to decrease slightly with increasing alteration. However, sample 11i does not follow this trend. Rather, it contains between 2.2 and 3.4 times more Ne-E than the other samples (Fig. 7). This shows that 11i had a much higher concentration of Ne-E carrying presolar SiC and/or graphite than the other samples.

Closed System Step Etching

In the CSSE analysis with oxidizing HNO_3, we expected to mainly release Q-gases as operationally defined. The compositions of Ar, Kr, and Xe indeed show that these gases are dominated by Q; however, significant Ne-E gases were released from presolar grains and the Ne isotopic compositions differ from that previously determined for Q. These results are outlined in more detail in the following paragraphs.

Both the isotopic compositions and the gas concentrations of Ar, Kr, and Xe are mostly in agreement with previous analyses of phase Q (Tables 6, 7, 9, S1 in supporting information; Fig. S3). Xenon was affected by some atmospheric contamination. After correction (Data S1), the concentration of $^{132}Xe_Q$ in the CSSE analysis of 11v is $(2.19 \pm 0.12) \times 10^{-7}$ cm^3STP/g IOM and $(2.45 \pm 0.21) \times 10^{-7}$ cm^3STP/g IOM in 5b, which are within uncertainty of each other. Adding the small amounts of $^{132}Xe_Q$ that remained in the residue after CSSE (7% of total $^{132}Xe_Q$ for 11v, 11% for 5b), we determine the total concentrations of $^{132}Xe_Q$ in the two IOM samples to be $(2.35 \pm 0.12) \times 10^{-7}$ cm^3STP/g IOM for 11v and $(2.72 \pm 0.22) \times 10^{-7}$ cm^3STP/g IOM for 5b. Note that these values could include small amounts of Xe-P3 in the oxidized residues, which is isotopically indistinguishable from Xe-Q in this data set.

The compositions of the light noble gases released in the CSSE analyses of the Tagish Lake samples differ more from each other and previous experiments than the composition of the heavy noble gases. The $^4He/^{36}Ar$ and $^{20}Ne/^{36}Ar$ ratios of the total gases released from the CSSE analyses compared to previous samples are shown in Fig. 9. This figure shows that the $^4He/^{36}Ar$ and $^{20}Ne/^{36}Ar$ ratios of the gases released from the HNO_3-susceptible material in 5b and 11v are relatively high compared to previous CSSE analyses and that 11v has higher $^4He/^{36}Ar$ and $^{20}Ne/^{36}Ar$ ratios than any previously analyzed sample. The gases released from HNO_3-susceptible phases in the more altered sample 11v have ~60% higher $^4He/^{36}Ar$ and ~30% higher $^{20}Ne/^{36}Ar$ ratios than those in the less altered sample 5b. This is in agreement with previous work that suggested that $^4He/^{36}Ar$ and $^{20}Ne/^{36}Ar$ in the HNO_3 susceptible phases in IOM are highest in meteorites that experienced aqueous alteration (Busemann et al. 2000).

The $^4He/^{36}Ar$ and $^{20}Ne/^{36}Ar$ ratios measured in individual etch steps show an interesting pattern in Fig. 6. In both etch runs, the earliest etch steps released gases with relatively high $^4He/^{36}Ar$ ratios; these ratios decreased in the gases in the intermediate steps to a minimum value in steps 14–16. The gases in the last etch steps had again higher $^4He/^{36}Ar$ and $^{20}Ne/^{36}Ar$ ratios. Interestingly, the last etch steps define a different slope than the early to intermediate steps. This indicates

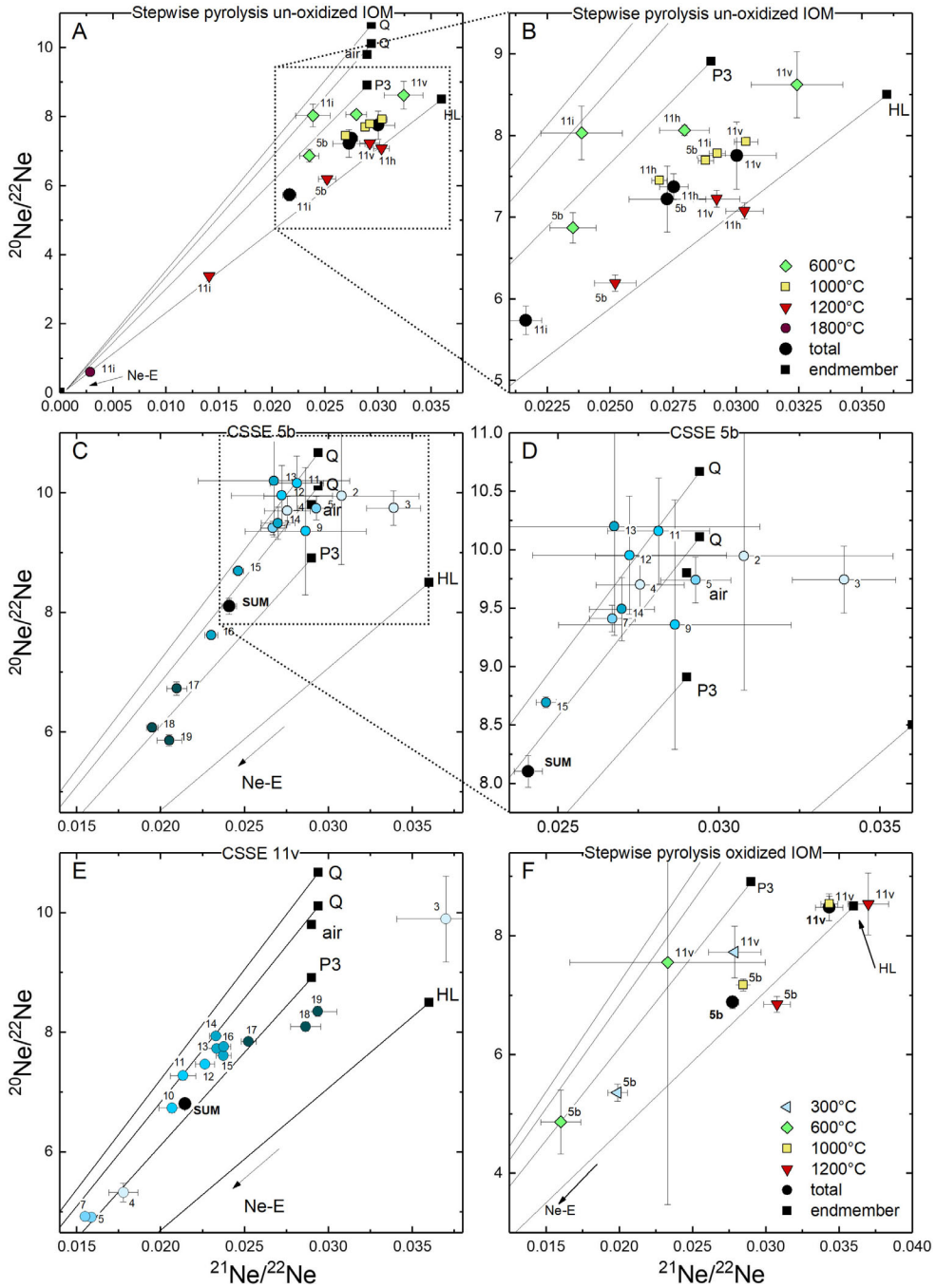

Fig. 5. Neon three isotope plots. A) Stepwise pyrolysis of unoxidized samples 5b, 11h, 11i, 11v. B) Enlarged area of (A). C) Neon released from HNO3-susceptible carriers during CSSE analysis of 5b. D) Enlarged area of (C). E) Neon released from HNO3-susceptible carriers during CSSE analysis of 11v. F) Neon released during stepwise heating of the oxidized IOM of 5b and 11v remaining after CSSE. Color image available in the digital version.

that a (sub-) phase with a lower He/Ne ratio but higher He/Ar and Ne/Ar ratios than the phase that released gases in the earlier etch steps released He and Ne in the last etch steps. The same has previously been seen in etch experiments of the CM2 chondrites Murchison (Wieler et al. 1992) and Cold Bokkeveld (Busemann et al. 2000).

Figures 5c–e show the Ne isotopic compositions of the gases released in the CSSE analyses. The Ne isotopic ratios differ significantly between 11v and 5b

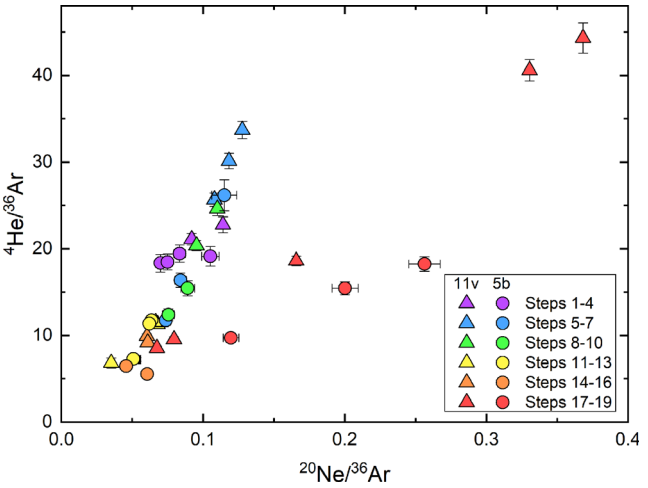

Fig. 6. ^{4}He/^{36}Ar versus ^{20}Ne/^{36}Ar of gases released in the two CSSE experiments. The gases released from 11v (triangles) and 5b (circles) plot in a similar patterns. In general, the ^{4}He/^{36}Ar and ^{20}Ne/^{36}Ar tend to decrease from step 1 to step 16 and increase from step 17 to step 19. Color image available in the digital version.

(Figs. 5c–e; Table 3). Most 5b etch steps have Ne isotopic compositions that scatter around the Q component. Only steps 15–19 have isotopic compositions that significantly deviate from previously determined values for phase Q. The isotopic compositions of 5b steps 15–19 are consistent with contributions from Ne-E, the relative contribution of Ne-E increasing with step number. In the 11v etch run, none of the etch steps have a Ne isotopic composition that is close to Q (Fig. 5e). All etch steps of 11v contain significant contributions from Ne-E. Neon-E has been observed previously in etch experiments and was attributed to the release of gases from presolar graphite grains (Wieler et al. 1992; Busemann et al. 2000).

The total He released in the two etch runs has a ^{3}He/^{4}He of $(1.40 \pm 0.02) \times 10^{-4}$ and $(1.83 \pm 0.01) \times 10^{-4}$ for 5b and 11v, respectively. Both values are similar to results from previous CSSE analyses, although higher than the lowest measured value for phase Q in Isna (CO3.8) of $(1.23 \pm 0.02) \times 10^{-4}$ (Busemann et al. 2000). This is likely due to variable minor amounts of cosmogenic ^{3}He in the Tagish Lake samples. The difference in the ^{3}He/^{4}He ratios in the two samples could be due to different shielding in the large Tagish Lake meteoroid (4–6 m in diameter; Brown et al. 2000).

Stepwise Pyrolysis of Oxidized IOM

The residues remaining after CSSE analysis, the oxidized IOM residues, were collected and analyzed using stepwise pyrolysis. Similar to the unoxidized IOM, the noble gases in the oxidized IOM are best understood as a mixture of Q-gases and gases carried by presolar grains: the HL, P3, and Ne-E components. However, since most of the noble gases in phase Q were released during the CSSE experiments, the primordial noble gas components carried by presolar grains are more prominent. This is well illustrated in the ^{4}He/^{132}Xe versus ^{20}Ne/^{132}Xe plot (Fig. 4); these ratios are much higher in the oxidized IOM than in the unoxidized IOM. The ^{36}Ar/^{132}Xe and ^{84}Kr/^{132}Xe ratios are also higher in the oxidized IOM than in the unoxidized IOM and in agreement with a mixture of Q and P3 gases (Fig. 3).

Figure 5f shows that the Ne isotopic compositions of the two oxidized IOM samples are in agreement with a mixture of HL, P3, and Ne-E and that the relative contributions of these components differ significantly between the two samples: Ne in 11v is completely dominated by Ne-HL while Ne in 5b has a much larger contribution of Ne-E. This is because the Ne-E gases were almost completely released from 11v during CSSE analysis while only ~35% of the total Ne-E in 5b was released (Fig. 7).

The HL component is also visible in the Xe isotopes (Fig. S3). The Xe data are roughly in agreement with 20% HL and 80% Q based on ^{132}Xe for 11v, and 10% HL and 90% Q for 5b. The concentration of $^{132}Xe_Q$ in the oxidized residues only accounts for ~10% of the total $^{132}Xe_Q$ in these samples, illustrating the efficient release of Xe-Q during CSSE. The concentration of $^{132}Xe_{HL}$ is estimated to be 3×10^{-9} cm^{3}STP/g IOM in both 11v and 5b, based on two-component deconvolution between HL and Q (^{136}Xe/$^{132}Xe_{HL}$ = 0.6991 [Huss and Lewis 1994; Ott 2014], ^{136}Xe/$^{132}Xe_Q$ = 0.3164 [Busemann et al. 2000]). This corresponds to 1–2% of the total primordial ^{132}Xe in the IOM.

Presolar SiC Abundance, Composition, and Size

The NanoSIMS study revealed that all samples but 11i have the same presolar SiC abundances within uncertainty, between 10 ± 5 and $14 + 3/-4$ ppm assuming 75 wt% matrix. The SiC abundance in 11i of 25 ± 5 ppm is about twice that of the other samples (Fig. 8; Table 4), indicating that the variable Ne-E concentrations between the samples (see the Stepwise Pyrolysis of Unoxidized IOM section) are due to heterogeneous SiC abundances. SiC abundances can also be calculated from the concentration of Ne-E in the unoxidized samples (Lewis et al. 1994; Huss and Lewis 1995) resulting in remarkably similar abundances to the NanoSIMS data (Table 4). The SiC abundances

Table 5. Concentration of all elements during stepwise pyrolysis as well as Ne isotopic composition.

Sample	Temperature (°C)	$^{4}He^{a}$	$^{36}Ar^{b}$	$^{84}Kr^{b}$	$^{132}Xe^{b}$	$^{22}Ne^{b}$	$^{20}Ne/^{22}Ne$	$^{21}Ne/^{22}Ne$
5b un ox	600	1.06 ± 0.06	1007 ± 340	9.1 ± 0.5	8.9 ± 0.5	5.9 ± 0.3	6.87 ± 0.19	0.0235 ± 0.0009
	1000	9.8 ± 0.5	1509 ± 168	12.3 ± 0.7	14.8 ± 0.8	36.6 ± 1.9	7.70 ± 0.05	0.0288 ± 0.0003
	1200	1.05 ± 0.06	480 ± 5	4.2 ± 0.3	5.5 ± 0.3	12.9 ± 0.7	6.19 ± 0.10	0.0252 ± 0.0008
	1800	0.0024 ± 0.0004	14.4 ± 0.1	0.3 ± 0.1	0.18 ± 0.03	0.3 ± 0.2	2.87 ± 2.30	0.0154 ± 0.0123
	Total	11.9 ± 0.5	3010 ± 379	25.9 ± 0.9	29.4 ± 1.0	55.6 ± 2.1	7.22 ± 0.41	0.0273 ± 0.0015
11h un ox	600	0.93 ± 0.01	450 ± 12	6.8 ± 0.1	7.30 ± 0.15	4.2 ± 0.1	8.07 ± 0.06	0.0279 ± 0.0010
	1000	9.8 ± 0.2	1472 ± 240	11.4 ± 0.2	13.8 ± 0.2	38.3 ± 0.6	7.45 ± 0.04	0.0269 ± 0.0003
	1200	1.06 ± 0.02	400 ± 6	3.4 ± 0.1	4.59 ± 0.08	10.8 ± 0.2	7.08 ± 0.10	0.0303 ± 0.0007
	1800	0.0075 ± 0.0004	72.1 ± 0.8	0.6 ± 0.1	0.85 ± 0.03	0.4 ± 0.1	9.75 ± 3.56	0.0320 ± 0.0126
	Total	11.8 ± 0.2	2402 ± 240	22.1 ± 0.3	26.6 ± 0.3	53.6 ± 0.7	7.37 ± 0.16	0.0275 ± 0.0006
11i un ox	600	0.63 ± 0.02	553 ± 229	6.0 ± 0.2	7.5 ± 0.2	3.7 ± 0.2	8.03 ± 0.33	0.0239 ± 0.0016
	1000	10.0 ± 0.3	1776 ± 482	11.9 ± 0.4	14.2 ± 0.4	37.8 ± 1.0	7.78 ± 0.04	0.0292 ± 0.0003
	1200	0.85 ± 0.02	310 ± 4	2.6 ± 0.1	3.65 ± 0.11	18.6 ± 0.5	3.38 ± 0.04	0.0141 ± 0.0003
	1800	0.0259 ± 0.0008	73.0 ± 0.8	0.6 ± 0.1	0.87 ± 0.04	6.9 ± 0.2	0.60 ± 0.05	0.0028 ± 0.0004
	Total	11.6 ± 0.3	2712 ± 533	21.0 ± 0.5	26.2 ± 0.5	68.1 ± 1.2	5.74 ± 0.17	0.0216 ± 0.0006
11v un ox	600	0.98 ± 0.05	597 ± 310	5.3 ± 0.3	6.0 ± 0.3	3.4 ± 0.2	8.62 ± 0.40	0.0324 ± 0.0018
	1000	11.7 ± 0.5	1476 ± 180	12.2 ± 0.6	14.2 ± 0.7	40.8 ± 1.9	7.93 ± 0.04	0.0304 ± 0.0005
	1200	1.18 ± 0.05	548 ± 9	4.7 ± 0.2	6.0 ± 0.3	11.9 ± 0.6	7.23 ± 0.10	0.0292 ± 0.0009
	1800	0.0063 ± 0.0004	48.6 ± 0.6	0.6 ± 0.1	0.56 ± 0.04	0.5 ± 0.2	5.57 ± 2.03	0.0205 ± 0.0090
	Total	13.8 ± 0.5	2669 ± 359	22.8 ± 0.7	26.8 ± 0.8	56.6 ± 2.0	7.76 ± 0.41	0.0300 ± 0.0016
5b ox	300	0.43 ± 0.01	259 ± 98	2.27 ± 0.08	1.40 ± 0.05	2.02 ± 0.07	5.36 ± 0.14	0.0199 ± 0.0007
	600	0.176 ± 0.006	65 ± 4	0.53 ± 0.03	0.27 ± 0.02	1.32 ± 0.07	4.87 ± 0.54	0.0160 ± 0.0014
	1000	6.0 ± 0.2	249 ± 92	1.41 ± 0.07	1.05 ± 0.04	20.59 ± 0.67	7.17 ± 0.10	0.0285 ± 0.0003
	1200	0.56 ± 0.02	39 ± 5	0.20 ± 0.06	0.24 ± 0.01	5.43 ± 0.19	6.85 ± 0.13	0.0308 ± 0.0009
	1800	0.0004 ± 0.0002	N/D	N/D	N/D	N/D	N/D	N/D
	Total	7.2 ± 0.2	612 ± 135	4.40 ± 0.12	2.96 ± 0.06	29.36 ± 0.70	6.89 ± 0.11	0.0277 ± 0.0004
11v ox	300	0.34 ± 0.01	130 ± 61	1.31 ± 0.05	0.99 ± 0.04	0.97 ± 0.04	7.73 ± 0.44	0.0279 ± 0.0018
	600	0.228 ± 0.008	43 ± 6	0.35 ± 0.05	0.20 ± 0.04	0.56 ± 0.12	7.56 ± 4.08	0.0233 ± 0.0067
	1000	6.6 ± 0.2	175 ± 38	0.86 ± 0.12	0.65 ± 0.04	18.14 ± 0.69	8.54 ± 0.13	0.0343 ± 0.0006
	1200	0.65 ± 0.02	37 ± 3	0.12 ± 0.12	0.19 ± 0.03	4.54 ± 0.23	8.54 ± 0.52	0.0370 ± 0.0014
	1800	0.0010 ± 0.0004	N/D	N/D	N/D	N/D	N/D	N/D
	total	7.9 ± 0.2	385 ± 72	2.64 ± 0.18	2.03 ± 0.07	24.20 ± 0.74	8.48 ± 0.23	0.0343 ± 0.0009

[a]Concentrations are given in 10^{-4} cm^3STP/g and calculated as cm^3STP/g of the total mass IOM loaded in the CSSE line.
[b]Concentrations are given in 10^{-8} cm^3STP/g and calculated as cm^3STP/g.

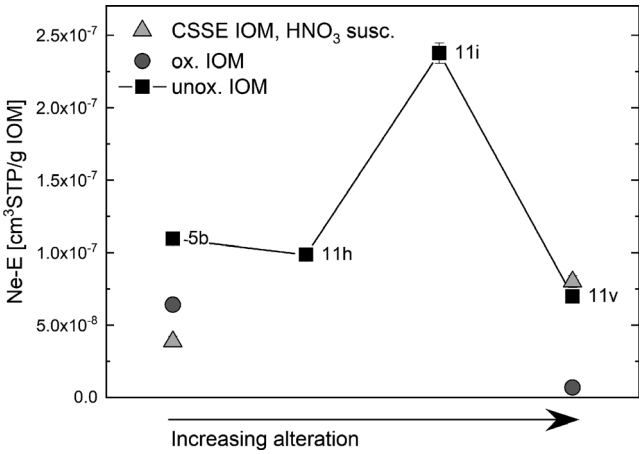

Fig. 7. The concentration of Ne-E in IOM analyzed in different ways. The black squares are the total concentration of Ne-E released during pyrolysis. The gray triangles are the total concentration of Ne-E released during the CSSE analysis with HNO_3. In 5b, ~30% of the Ne-E released during pyrolysis was released during CSSE analysis. In contrast, in 11v, essentially all the Ne-E was released during CSSE analysis with HNO_3. The Ne-E concentrations in the residues remaining after HNO_3 treatment are shown as circles. The oxidized residue of 11v is essentially void of Ne-E whereas the oxidized residue of 5b released significant amounts of Ne-E.

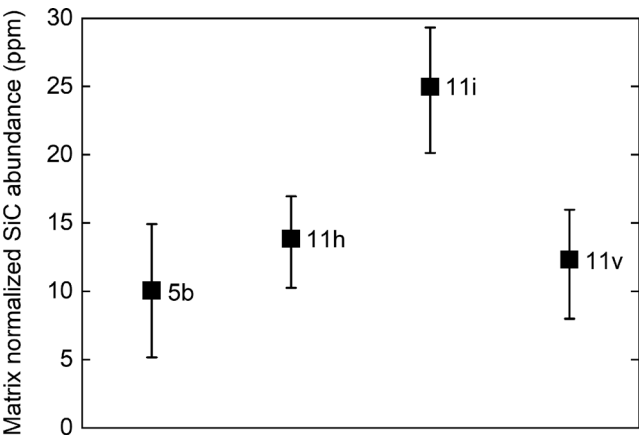

Fig. 8. Matrix normalized abundances of SiC grains in the four IOM samples based on NanoSIMS mapping.

of 5b, 11h, and 11v (10–14 ppm) are lower than the typical abundance in primitive chondrites determined by Davidson et al. (2014) to be ~30 ppm. However, as the matrix abundance in Tagish Lake is uncertain, comparison with literature data is not straightforward. If 40 wt% matrix is assumed instead of 75 wt%, then 5b, 11h, and 11v would have matrix-normalized SiC abundances of 25–32 ppm.

In addition to the SiC abundances, the NanoSIMS study also provided SiC grain sizes and C isotopic compositions. There is no difference in the size

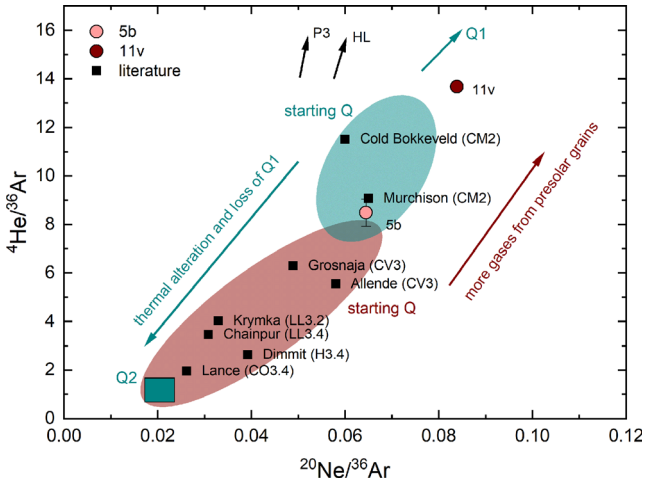

Fig. 9. $^4He/^{36}Ar$ and $^{20}Ne/^{36}Ar$ ratios of the gases released during CSSE of IOM in this and previous studies (Wieler et al. 1991, 1992; Busemann et al. 2000; Riebe et al. 2013). The most aqueously altered samples have the highest $^4He/^{36}Ar$ and $^{20}Ne/^{36}Ar$ ratios in the gases released during CSSE. Busemann et al. (2000; turquoise markings) interpreted this observation as Q having two subcomponents. Q1 with higher $^4He/^{36}Ar$ and $^{20}Ne/^{36}Ar$ ratios would be lost during thermal metamorphism but not during aqueous alteration and the higher ratios in the more aqueously altered samples are considered pristine. Following this interpretation, the two Tagish Lake samples are expected to have similar $^4He/^{36}Ar$ and $^{20}Ne/^{36}Ar$ ratios. However, the gases in the more altered sample 11v had higher ratios than those in the less altered sample 5b. In light of this new data set, we suggest that the variations of the ratios might not be variations in Q proper, but rather addition of gases from presolar nanodiamonds with higher $^4He/^{36}Ar$ and $^{20}Ne/^{36}Ar$ ratios (red markings). Color image available in the digital version.

distribution of SiC grains in the different samples (Fig. S5). The average grain size is around 250–300 nm, smaller than the average size of between 300 and 770 nm recorded by Davidson et al. (2014) for various meteorite groups. The C isotopes in SiC grains provide information on the types of stars around which the grains formed (Zinner 2014). More information about the parent stars can be deduced when the isotopic compositions of more than one element are known. Hence, the N isotopes were measured along with C during mapping. However, the count rates were too low to provide reliable $^{14}N/^{15}N$ ratios for the SiC grains. All of the SiC grains analyzed in the Tagish Lake samples have $^{12}C/^{13}C$ ratios similar to those of mainstream SiC grains originating from asymptotic giant branch (AGB) stars (Fig. S1; Table 4; Lambert et al. 1986). In Fig. S1, it is seen that the $^{12}C/^{13}C$ ratios of Tagish Lake grains are skewed toward the Tagish Lake IOM value of $^{12}C/^{13}C = 90$ (Alexander et al. 2014) compared to mainstream SiC grains that were isolated from IOM.

Table 6. Isotopic composition of He, Ar, and Kr of total release in the different analyses of different samples.

	$^{3}He/^{4}He \times 10^{-4}$	$^{38}Ar/^{36}Ar$	$^{40}Ar/^{36}Ar$	$^{82}Kr/^{84}Kr$	$^{83}Kr/^{84}Kr$	$^{86}Kr/^{84}Kr$
Unoxidized IOM						
5b	1.40 ± 0.01	0.190 ± 0.004	5.5 ± 0.6	0.197 ± 0.003	0.199 ± 0.003	0.277 ± 0.007
11h	1.41 ± 0.01	0.188 ± 0.004	2.0 ± 0.1	0.202 ± 0.003	0.202 ± 0.003	0.278 ± 0.009
11i	1.41 ± 0.01	0.188 ± 0.008	1.7 ± 0.2	0.201 ± 0.004	0.203 ± 0.004	0.307 ± 0.006
11v	1.75 ± 0.01	0.189 ± 0.004	5.7 ± 0.6	0.203 ± 0.003	0.201 ± 0.003	0.304 ± 0.005
HNO_3-susceptible (CSSE)						
5b	1.40 ± 0.02	0.189 ± 0.002	2.92 ± 0.04	0.203 ± 0.003	0.202 ± 0.003	0.304 ± 0.004
11v	1.83 ± 0.01	0.187 ± 0.001	3.13 ± 0.02	0.202 ± 0.006	0.201 ± 0.006	0.306 ± 0.008
Oxidized IOM						
5b	1.48 ± 0.02	0.191 ± 0.005	4.7 ± 0.4	0.202 ± 0.007	0.205 ± 0.007	0.303 ± 0.010
11v	1.69 ± 0.02	0.191 ± 0.007	1.9 ± 1.2	0.193 ± 0.018	0.193 ± 0.018	0.292 ± 0.028
Q*	1.23 ± 0.02	0.1873 ± 0.0007		0.2018 ± 0.0002	0.2018 ± 0.0002	0.3095 ± 0.0005

*Isotopic composition of Q from Busemann et al. (2000).

This is because the $^{12}C/^{13}C$ ratios of the grains are affected by dilution from the surrounding IOM (cf. Davidson et al. 2014). Due to the dilution, SiC grains with measured $^{12}C/^{13}C$ ratios lower than 90 are overestimated and those with $^{12}C/^{13}C$ ratios higher than 90 are underestimated.

DISCUSSION

The main motivation for this work was to investigate the effects of aqueous alteration on primordial noble gases and their carriers. Ideal for this purpose, the four Tagish Lake samples have been extensively studied previously, both as bulk samples and the extracted IOM (Herd et al. 2011; Alexander et al. 2014; Blinova et al. 2014a, 2014b; Quirico et al. 2018). The petrology, mineralogy, and bulk O isotopes of the samples all show that the four samples are from the same parent body, that is, that none of them are foreign clasts, and that the observed differences are the result of variable aqueous alteration (Herd et al. 2011, 2012; Alexander et al. 2014; Blinova et al. 2014b). A recent study using thermogravimetric analysis and infrared spectroscopy of these and other Tagish Lake clasts demonstrates this relationship and indicates that Tagish Lake alteration is similar to that experienced by lesser altered CM chondrites (Gilmour et al. 2019). Differences in IOM functional group chemistry and elemental and isotopic compositions between the different samples are well understood as the consequence of variable alteration, most likely due to differences in peak temperature (<<600 °C) experienced during aqueous alteration and/or duration of alteration (Alexander et al. 2014; Quirico et al. 2018). Alexander et al. (2014) suggested that variable alteration conditions could be achieved on the same parent body if (1) Tagish Lake is a breccia with clasts from different parts of a larger parent body or (2) the variable alteration occurred next to a local heat source such as a fracture with hot fluid flow or an igneous intrusion. Quirico et al. (2018) noted that a low pressure shock (<10 GPa) could also produce the properties observed in the Tagish Lake samples, although independent evidence for shock in the Tagish Lake samples has not been reported.

There are only moderate differences in the concentrations of primordial noble gases between the Tagish Lake samples in this study, reflecting that the differences in aqueous alteration did not result in major gas loss from the IOM (Fig. S4). The range of trapped ^{36}Ar ($^{36}Ar_{tr}$) in the Tagish Lake IOM sample of 0.67–0.72×10^{-6} cm^3STP/g meteorite (recalculated based on the yields in Table 2) is narrow. Significantly larger variations of between 0.5 and 1.1×10^{-6} cm^3STP/g meteorite, decreasing with alteration, have been observed in bulk CM chondrites (Marrocchi et al. 2014; Weimer et al. [2017] and references therein). However, the Ar that is lost during aqueous alteration of bulk CM chondrites might reside in the soluble portion of meteorites (e.g., Matsuda et al. 1980) and would hence be destroyed during IOM preparation. In contrast, the Q component should be mostly retained in the IOM. The concentration of $^{132}Xe_Q$ in samples 5b and 11v are similar ($[2.35 \pm 0.12] \times 10^{-7}$ cm^3STP/g for 11v and $[2.72 \pm 0.22] \times 10^{-7}$ cm^3STP/g for 5b), showing that loss of Q-gases must have been minor if it occurred during aqueous alteration. Alteration on the Tagish Lake parent body still resulted in significant modifications to the noble gases and their carriers, including gas loss from presolar grains and changes in the HNO_3 susceptibility of presolar grains. In addition, this study shows that the distribution of presolar SiC

Table 7. Isotopic composition of Xe of total release in the different analyses of different samples.

	$\frac{^{124}Xe}{^{132}Xe}$	$\frac{^{126}Xe}{^{132}Xe}$	$\frac{^{128}Xe}{^{132}Xe}$	$\frac{^{129}Xe}{^{132}Xe}$	$\frac{^{130}Xe}{^{132}Xe}$	$\frac{^{131}Xe}{^{132}Xe}$	$\frac{^{134}Xe}{^{132}Xe}$	$\frac{^{136}Xe}{^{132}Xe}$
Unoxidized IOM								
5b	0.00493 ± 0.00007	0.00434 ± 0.00008	0.0818 ± 0.0009	1.045 ± 0.011	0.161 ± 0.002	0.816 ± 0.009	0.382 ± 0.004	0.322 ± 0.003
11h	0.00467 ± 0.00005	0.00419 ± 0.00007	0.0813 ± 0.0009	1.028 ± 0.011	0.160 ± 0.002	0.817 ± 0.008	0.380 ± 0.004	0.322 ± 0.003
11i	0.00457 ± 0.00007	0.00421 ± 0.00006	0.0810 ± 0.0009	1.026 ± 0.011	0.160 ± 0.002	0.816 ± 0.009	0.383 ± 0.004	0.322 ± 0.003
11v	0.00477 ± 0.00006	0.00425 ± 0.00007	0.0820 ± 0.0009	1.048 ± 0.010	0.161 ± 0.002	0.819 ± 0.008	0.383 ± 0.004	0.322 ± 0.003
HNO_3-susceptible (CSSE)								
5b	0.00448 ± 0.00006	0.00402 ± 0.00005	0.0800 ± 0.0010	1.028 ± 0.012	0.160 ± 0.002	0.814 ± 0.010	0.380 ± 0.005	0.318 ± 0.004
11v	0.00431 ± 0.00005	0.00388 ± 0.00005	0.0791 ± 0.0008	1.023 ± 0.011	0.159 ± 0.002	0.811 ± 0.009	0.381 ± 0.004	0.320 ± 0.003
Oxidized IOM								
5b	0.00514 ± 0.00012	0.00476 ± 0.00011	0.0822 ± 0.0017	1.044 ± 0.021	0.161 ± 0.003	0.815 ± 0.016	0.405 ± 0.008	0.352 ± 0.007
11v	0.00557 ± 0.00035	0.00506 ± 0.00031	0.0822 ± 0.0045	1.055 ± 0.058	0.161 ± 0.009	0.831 ± 0.046	0.419 ± 0.023	0.379 ± 0.021
Q*	0.00455 ± 0.00002	0.00406 ± 0.00002	0.0822 ± 0.0002	1.042 ± 0.002	0.1619 ± 0.0003	0.8185 ± 0.0009	0.378 ± 0.001	0.3154 ± 0.0008

*Isotopic composition of Q from Busemann et al. (2000).

Table 8. Concentration of Ne-E.

Sample	cm^3STP/g IOM	cm^3STP/g meteorite*
5b unox	$1.1 \times 10^{-7} \pm 4.5 \times 10^{-9}$	1.7×10^{-9}
11h unox	$9.8 \times 10^{-8} \pm 2.9 \times 10^{-9}$	1.8×10^{-9}
11i unox	$2.4 \times 10^{-7} \pm 8.6 \times 10^{-9}$	4.3×10^{-9}
11v unox	$7.0 \times 10^{-8} \pm 3.0 \times 10^{-9}$	1.2×10^{-9}
11v etch	$8.0 \times 10^{-8} \pm 4.1 \times 10^{-9}$	
5b etch	$3.9 \times 10^{-8} \pm 3.9 \times 10^{-9}$	
11v ox	$7.0 \times 10^{-9} \pm 6.2 \times 10^{-10}$	
5b ox	$6.4 \times 10^{-8} \pm 1.6 \times 10^{-9}$	

*Calculated to per g meteorite using yields in Alexander et al. (2014). See supporting information for details on deconvolution.

grains is heterogeneous, either due to indigenous heterogeneity between the samples or due to redistribution during parent body processing.

SiC Abundance Variation

The abundance of presolar SiC grains in the different Tagish Lake samples vary so that the second most altered sample 11i has an abundance of SiC grains that is about twice that of the other samples based on NanoSIMS mapping (Fig. 8). As a comparison, all the CR chondrites that Davidson et al. (2014) analyzed had similar SiC abundances (see their fig. 4). The noble gas data also show the uneven distribution of SiC between the samples: 11i has a two to three times higher concentration of Ne-E than the other samples (Fig. 7). Ne-E is carried by both presolar graphite (Ne-E[L]) and SiC (Ne-E[H]; Table 1), the two carriers having different release temperatures during stepwise heating: Ne-E(L) is released from graphite ≤900 °C, while Ne-E (H) is released from SiC >900 °C (Eberhardt et al. 1981). The resolution of the stepwise heating in this study is not high enough to clearly distinguish between Ne-E(L) and Ne-E(H). Nevertheless, the Ne-E release pattern in Fig. 10 shows that the excess Ne-E in sample 11i (compared to the other samples) is mainly released in the 1200 °C and the 1800 °C steps, a strong indication that the excess Ne-E in 11i is carried by presolar SiC.

We have identified three possible explanations for the higher abundance of SiC grains in the second most altered sample 11i (1) preferential destruction of IOM over SiC during the alteration in 11i, (2) heterogeneous accretion of SiC grains, (3) redistribution of SiC grains on the parent body during aqueous alteration. Explanation (1), that IOM was preferentially destroyed over SiC during alteration, can almost certainly be excluded as the samples have very similar abundances of IOM C, inconsistent with a substantial loss of IOM from the more altered samples (Alexander et al. 2014).

The second potential explanation for the higher abundance of SiC grains in sample 11i is that the accretion of SiC grains to the Tagish Lake parent body was heterogeneous. There is compelling evidence that different meteorite groups accreted matrix with a similar mixture of presolar grains and IOM and that the observed differences between meteorites and meteorite groups are due to parent body processing (Alexander 2005; Davidson et al. 2014). Other authors have argued that nebular processing, in addition to parent body processing, was important in establishing differences of presolar grain abundances between different meteorite classes (Huss and Lewis 1995; Huss et al. 2003). The differences in presolar grain abundances between samples from the same group have, however, almost exclusively been assigned to parent body alteration (Huss and Lewis 1995; Huss et al. 2003; Alexander 2005; Davidson et al. 2014). The abundance of IOM C is constant between the different Tagish Lake samples, showing that the samples had similar matrix abundances (Alexander et al. 2014). Assuming a constant SiC fraction in matrix (Alexander 2005; Davidson et al. 2014), the samples would have accreted similar concentrations of SiC. The different Tagish Lake samples also have similar concentrations of major, minor, and trace elements, which shows that the Tagish Lake starting material was mostly homogeneous (Blinova et al. 2014b). The heterogeneous distribution of presolar SiC in Tagish Lake could have occurred during accretion but with the currently available data, it is unclear why such heterogeneity would have occurred during the accretion of Tagish Lake and not during the accretion of other asteroids such as the CR chondrite parent body (Davidson et al. 2014).

The third potential explanation for the heterogeneous distribution of presolar SiC grains in Tagish Lake is that aqueous alteration redistributed SiC grains on the Tagish Lake parent body. If parent body modification is responsible for the heterogeneous distribution of SiC grains, then either sample 11i became enriched in SiC grains during the alteration or samples 5b, 11h, and 11v all lost SiC grains to the same degree. The calculated abundance of SiC grains in the samples depends largely on the amount of matrix in the samples (see the NanoSIMS section). For the 75% matrix assumed here, the abundance of SiC in 11i of 25 ± 4 ppm is similar to the abundance of ~30 ppm determined for primitive meteorites by Davidson et al. (2014), while the abundance of 10–14 ppm determined for the other Tagish Lake samples differs significantly from the Davidson value. However, it seems unlikely that samples 5b, 11h, and 11v, which experienced different degrees of alteration, lost the same amount of SiC grains, especially since sample 5b appears to be

Table 9. Concentration of major isotopes in individual steps in CSSE analyses of 5b and 11v.

Step	5b $^{4}He^{a}$	$^{36}Ar^{a}$	$^{84}Kr^{b}$	$^{132}Xe^{b}$	11v $^{4}He^{a}$	$^{36}Ar^{a}$	$^{84}Kr^{b}$	$^{132}Xe^{b}$
1	0.98 ± 0.05	0.060 ± 0.002	0.86 ± 0.05	0.95 ± 0.05	0.58 ± 0.02	0.0255 ± 0.0008	0.31 ± 0.02	0.48 ± 0.03
2	3.0 ± 0.1	0.186 ± 0.007	0.68 ± 0.04	0.78 ± 0.04	2.38 ± 0.06	0.113 ± 0.003	0.72 ± 0.04	0.90 ± 0.05
3	12.7 ± 0.5	0.75 ± 0.02	1.28 ± 0.07	1.60 ± 0.09	10.3 ± 0.2	0.400 ± 0.010	0.94 ± 0.05	1.28 ± 0.07
4	14.4 ± 0.6	0.84 ± 0.03	1.00 ± 0.06	1.30 ± 0.07	16.1 ± 0.4	0.48 ± 0.01	0.76 ± 0.04	1.06 ± 0.06
5	15.2 ± 0.6	1.12 ± 0.04	1.6 ± 0.1	2.3 ± 0.1	27.8 ± 0.7	0.92 ± 0.02	1.3 ± 0.1	1.8 ± 0.2
6	0.66 ± 0.04	0.033 ± 0.001	0.105 ± 0.007	0.113 ± 0.007	1.60 ± 0.04	0.065 ± 0.002	0.06 ± 0.05	0.15 ± 0.03
7	23.4 ± 1.0	2.00 ± 0.07	2.2 ± 0.1	2.7 ± 0.2	54 ± 1	2.67 ± 0.06	4.3 ± 0.3	3.7 ± 0.2
8	N/D	N/D	N/D	N/D	N/D	N/D	N/D	N/D
9	2.15 ± 0.09	0.141 ± 0.005	0.09 ± 0.01	0.23 ± 0.02	0.115 ± 0.008	0.017 ± 0.001	5.9 ± 0.4	1.44 ± 0.10
10	1.25 ± 0.05	0.102 ± 0.004	0.70 ± 0.05	0.66 ± 0.04	6.2 ± 0.1	0.55 ± 0.01	0.64 ± 0.03	0.88 ± 0.05
11	6.5 ± 0.3	0.60 ± 0.02	0.44 ± 0.03	0.46 ± 0.03	6.6 ± 0.2	0.57 ± 0.01	0.58 ± 0.03	0.72 ± 0.04
12	4.6 ± 0.2	0.62 ± 0.02	0.61 ± 0.04	0.79 ± 0.05	14.1 ± 0.3	1.42 ± 0.03	1.42 ± 0.07	1.75 ± 0.09
13	3.1 ± 0.1	0.49 ± 0.01	0.25 ± 0.01	0.29 ± 0.02	17.9 ± 0.4	1.95 ± 0.05	3.2 ± 0.2	3.1 ± 0.2
14	7.3 ± 0.3	1.13 ± 0.04	1.06 ± 0.06	1.25 ± 0.07	34.7 ± 0.8	4.8 ± 0.1	4.8 ± 0.3	5.9 ± 0.3
15	50 ± 2	*8.53 ± 1.45*[c]	*8 ± 1*[c]	*11 ± 3*[c]	18.3 ± 0.4	2.14 ± 0.05	2.6 ± 0.1	3.0 ± 0.2
16	18.9 ± 0.8	3.82 ± 0.11	3.6 ± 0.2	5.1 ± 0.3	14.1 ± 0.3	1.48 ± 0.04	1.43 ± 0.08	1.8 ± 0.1
17	5.7 ± 0.2	0.59 ± 0.02	0.69 ± 0.04	1.09 ± 0.06	23.5 ± 0.6	1.26 ± 0.03	2.0 ± 0.1	2.4 ± 0.1
18	13.7 ± 0.6	0.88 ± 0.03	0.88 ± 0.05	0.97 ± 0.06	8.2 ± 0.2	0.203 ± 0.005	0.35 ± 0.02	0.33 ± 0.02
19	4.0 ± 0.2	0.220 ± 0.007	0.24 ± 0.01	0.30 ± 0.02	5.9 ± 0.1	0.134 ± 0.005	0.27 ± 0.02	0.27 ± 0.01
Total	188 ± 3	22 ± 1	24 ± 1	31 ± 3	263 ± 2	19.2 ± 0.2	25.8 ± 0.5	30.8 ± 0.5

Numbers in italics are calculated and less certain than other values.

[a]Concentrations are given in 10^{-6} cm^3STP/g and calculated as cm^3 STP/g of the total mass IOM loaded in the CSSE line.

[b]Concentrations are given in 10^{-8} cm^3STP/g and calculated as cm^3STP/g of the total mass IOM loaded in the CSSE line.

[c]Concentration of ^{36}Ar, ^{84}Kr, and ^{132}Xe in step 15 was calculated based on ratios with ^{4}He and ^{20}Ne of steps 14 and 16 and the concentration of ^{4}He and ^{20}Ne in step 15.

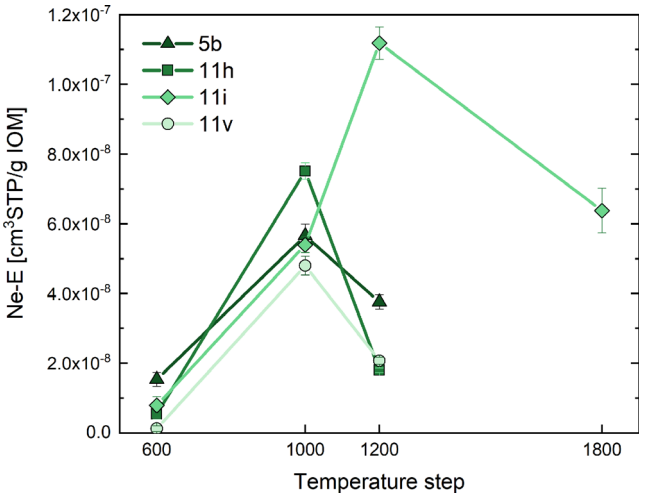

Fig. 10. Release pattern of Ne-E during stepwise heating of unoxidized IOM. The samples release less gases in the 600 °C step with increasing alteration, indicating that the Ne-E(L) gases might be lost from presolar graphite during alteration. Sample 11i had a significantly higher concentration of Ne-E (H) than the other samples. The excess Ne-E gases in 11i compared to the other samples was released in the 1200 and 1800 °C steps, evidence that the gases originated from presolar SiC (Ne-E[H]) and not presolar graphite (Ne-E[L]). Color image available in the digital version.

much less altered than the other samples (Quirico et al. 2018), making it implausible that SiC grains were destroyed in sample 5b during alteration. For this discussion, we will therefore assume that 11i is the anomaly, due to a redistribution rather than the destruction of SiC grains on the Tagish Lake parent body.

The redistribution of SiC grains in the Tagish Lake parent body would require significant fluid flow. The O isotopic compositions of the Tagish Lake samples are in agreement with either a closed system equilibrium interaction with different water/rock ratios or an open system, in which water was redistributed between different parts of the parent body (Herd et al. 2012). The initial water/rock ratio of Tagish Lake has been estimated to be similar to that of CM chondrites (Alexander 2019). The presence of large pyrrhotite veins in a CM1 clast in Tagish Lake appears to be evidence of significant fluid transfer (Zolensky et al. 2002; Bullock et al. 2005), although alteration of this foreign clast might have occurred prior to incorporation into Tagish Lake. There is some evidence in the literature for the redistribution of mobile elements (Ba, Sr) and decrease of volatile elements (Cd, Sb) with increased alteration (Blinova et al. 2014b). Taken together, these results indicate that the fluid flow in Tagish Lake might have been relatively high. However, due to seemingly conflicting evidence, there is no consensus on the extent of fluid flow during aqueous alteration or what a high fluid flow would mean in terms of mobility (e.g., Young et al. 1999; Bland et al. 2009; Palguta et al. 2010; Brearley 2014; Bland and Travis 2017).

Closed system alteration with stagnant pore water is supported by petrological studies, which tend to conclude that mobility of elements was restricted to 100s of μm (for a review, see Brearley 2014). The stagnant pore water model is also in agreement with the high concentrations of volatile elements in chondrites and the low variability of soluble element concentrations. In an open system, volatile elements would have been lost to a higher degree (see Bland et al. 2009; Brearley 2014). Other observations are better explained by open system behavior during aqueous alteration. For example, variations in the O isotopic compositions of carbonates require variable temperature and/or water/rock ratios and have been taken as an indication of open system alteration with fluid convection in the parent body (Young et al. 1999). Bland and Travis (2017) suggested that most observations could be explained by a model in which alteration of CM chondrites is described as having occurred in convecting mud balls instead of in lithified rock as modeled previously. In the mud ball model, particle transportation and even size sorting of chondrules can occur while there is little loss of volatile elements, and mobile elements remain homogeneously distributed throughout the parent body (Bland and Travis 2017). Perhaps, the mud ball model could also result in sorting of small dense SiC grains, although the behavior of small dense grains was not investigated in the Bland and Travis paper.

We currently have insufficient data to determine whether the variation in SiC abundance between the different samples is an effect of heterogeneous accretion or redistribution during aqueous alteration. Further studies such as in situ NanoSIMS isotopic mapping of the distribution of SiC grain in thin sections of the samples would be required for a better understanding of this issue.

Changes in HNO_3-Susceptibility and Degassing Behavior of Presolar Grains

The alteration of Tagish Lake resulted in degassing of presolar graphite grains and changed the susceptibility of presolar SiC grains and likely nanodiamonds to HNO_3 and, consequently, the perceived composition of the noble gas component Q. We discuss the effects of aqueous alteration on different presolar grains below.

SiC and Graphite

Both presolar SiC and graphite were affected by the alteration; the most prominent effect on SiC is an increased susceptibility to HNO_3 etching, whereas graphite seems to have been partially degassed during the alteration. We can use the release temperature during stepwise heating to distinguish between the isotopically very similar Ne-E(H) component in SiC with a release temperature >900 °C and Ne-E(L) in graphite with a release temperature ≤900 °C (Eberhardt et al. 1981). The unoxidized residue of the least altered sample, 5b, released a significant amount of its total Ne-E gases in the 600 °C step (~15%, 1.5×10^{-8} cm^3STP/g IOM, Fig. 10), that is, Ne-E(L) gases, which likely originated from graphite. Samples 11h and 11i that experienced intermediate parent body alteration released less Ne-E(L) gases and the most altered sample 11v contained no resolvable Ne-E in the 600 °C step (Figs. 5a, 5b, and 10). It, therefore, appears that parent body alteration of the Tagish Lake samples resulted in progressive loss of Ne-E gases related to presolar graphite.

The increased susceptibility of aqueously altered presolar SiC to HNO_3 etching is seen in the CSSE analyses and in the comparison between the amounts of Ne-E gases released in the CSSE analysis and the stepwise heating. Ne-E was clearly visible in the CSSE analyses of both the less altered sample 5b and the more altered sample 11v (Figs. 5c–e). There is, however, a clear difference in the amounts of Ne-E in the two analyses. Essentially, the full budget of Ne-E, as estimated from the stepwise heating of the unoxidized IOM, was released from the 11v sample during etching with HNO_3 in the CSSE analysis, whereas only ~35% of the Ne-E in 5b was released (Fig. 7; Table 8). It is, therefore, clear that the more altered sample 11v released all Ne-E from both graphite and SiC during etching with HNO_3, while the less altered sample 5b retained the majority of the Ne-E gases. The Ne-E released from 5b could (1) be exclusively from presolar graphite or (2) be released from presolar graphite and SiC. Previous CSSE experiments of IOM samples of Chainpur (LL3.4), Cold Bokkeveld (CM2; Busemann et al. 2000), and Murchison (CM2) (Wieler et al. 1992) also released Ne-E, assumed to be Ne-E(L) from graphite (Wieler et al. 1992; Busemann et al. 2000).

Sample 5b released 3.9×10^{-8} cm^3STP/g Ne-E during the CSSE analysis, more than twice the Ne-E released from graphite in the 600 °C step during stepwise heating. However, the 1000 °C step likely contains a mixture of Ne-E from both graphite and SiC, and we cannot determine if the Ne-E released during CSSE of 5b was exclusively hosted in graphite or was released from both graphite and SiC. The SiC grains in 11v were not largely degassed during alteration (Fig. 7); however, their increased susceptibility to HNO_3 likely represents a step toward degassing. Aqueous alteration that was more severe and/or involved more corrosive conditions can likely result in complete degassing of SiC grains. Davidson et al. (2014) found that the concentration of SiC grains in the CR2 chondrite Renazzo determined by NanoSIMS imaging is higher than concentrations determined by noble gases (Huss et al. 2003) and suggested that parent body alteration might have degassed the presolar SiC grains in Renazzo.

Huss et al. (2003) suggested that there might be a second carrier of Ne-E(H) in addition to SiC based on two observations. (1) The inferred concentration of SiC was considerably higher by ~50% in CM2 chondrites than in CI chondrites based on Ne-E(H) in oxidized residues, and (2) a previous study (Huss and Lewis 1995) had shown that the unoxidized residue of Orgueil (CI) contained about 70% more Ne-E(H) than the oxidized residue of the same sample. Both these observations are in agreement with the observation in this study and could be explained by changes in HNO_3 susceptibility of presolar SiC grains during aqueous alteration. CI chondrites are more aqueously altered than CM2 chondrites, and hence could carry Ne-E in SiC that is even more susceptible to oxidation than the SiC in CM2 chondrites. We therefore suggest that an additional carrier of Ne-E(H) is not needed, and that the simplest interpretation of the data is that parent body aqueous alteration affects SiC such that it more readily releases its gases during oxidation in the laboratory. Huss and Lewis (1995) suggested that Orgueil could contain two subpopulations of SiC: one that is more reactive, perhaps due to radiation damage and releases its gases during etching, and one that is more refractory and survives thermal metamorphism better. The first population would only survive in meteorites with very low metamorphic temperatures. Huss and Lewis (1995) also observed SiC grains that were susceptible to etching in the LL3.5 chondrite Ragland, for which they suggested that alteration on the parent body might have changed the physical properties of some SiC grains so that they became more susceptible to etching, similar to what we found in this study.

Nanodiamonds

Although less conclusive, there is some evidence that the presolar nanodiamonds in Tagish Lake also became more susceptible to etching with HNO_3 with increasing aqueous alteration, similar to presolar SiC. The $^4He/^{36}Ar$ and $^{20}Ne/^{36}Ar$ ratios of the gases released during CSSE are higher in the more altered

sample 11v than in the less altered sample 5b (Fig. 9). The difference in the ratios is a result of a combination of more He and Ne and less Ar released in the CSSE analysis of 11v compared to 5b (Fig. S6 in supporting information). Noble gases in presolar grains have significantly higher He/Ar and Ne/Ar ratios than noble gases in phase Q (Ott 2014) and it seems likely that the additional He and Ne in the 11v HNO_3 susceptible material originated from presolar grains. Ne-E was likely released from graphite in both samples during CSSE, and we can, therefore, rule out that these gases contributed to the differences in elemental ratios. Based on the $^4He/^{22}Ne$ ratio in presolar SiC (Lewis et al. 1994) and the concentration of Ne-E released from 11v in the CSSE experiment, at most a few percent of the ^4He is expected to have been released from SiC. Presolar nanodiamonds are the main carriers of He and Ne in Tagish Lake IOM (Figs. 4 and 5a, 5b, 5f) and it seems plausible that small amounts of He and Ne could have been released from the nanodiamonds during the CSSE analysis. The same mechanism that modified SiC during aqueous alteration might have modified the nanodiamonds so that they became somewhat more susceptible to the HNO_3 treatment in the more altered sample 11v than the less altered sample 5b.

Another interesting feature of the elemental ratios in the gases released during the CSSE experiments is that the last etch steps in both CSSE analyses have high $^4He/^{36}Ar$, $^{20}Ne/^{36}Ar$, and $^{20}Ne/^4He$ ratios (Fig. 6) compared to the earlier steps. The same was observed in similar experiments on Murchison (CM2; Wieler et al. 1992) and to some degree also in Cold Bokkeveld (CM2; Busemann et al. 2000). Wieler et al. (1992) interpreted the late increase in these ratios as release of gas from another component in addition to Q and suggested that this HNO_3-susceptible carrier contained gases related to HL. Interestingly, the 1200 °C step in both the unoxidized and the oxidized IOM of all samples has higher $^{20}Ne/^4He$ ratios than the 1000 °C step (Fig. 4). It is possible that the same component with high $^{20}Ne/^4He$ was released in the 1200 °C heating steps and in the last etch steps. Apparently, this phase is more susceptible to oxidation and less resistant to heating than bulk HL proper. More data are needed to deduce if this phase is only present in CM2 chondrites and Tagish Lake, or if it is always present but only releases noble gases during treatment with HNO_3 in aqueously altered samples. It would, for example, be interesting to see if CSSE analysis of IOM from the meteorite Paris, which has been suggested to be the least altered CM chondrite (Marrocchi et al. 2014), releases gases in the last etch steps with high $^4He/^{36}Ar$ and $^{20}Ne/^{36}Ar$ ratios.

Q and Other Components Released by CSSE

The data in this study highlight the difficulty with the operational definition of phase Q (Lewis et al. 1975). According to this definition, phase Q is concentrated in IOM residues compared to bulk meteorites and releases the Q-gases when exposed to HNO_3 or other oxidizing agents. With the CSSE analyses, we analyzed phase Q as operationally defined. However, the gases released with CSSE differed significantly from the composition of Q-gases determined previously (Busemann et al. 2000). As discussed above, we attribute these differences to gas release from presolar grains. Most prominent were the Ne-E gases released from presolar SiC and graphite that obscured the Ne isotopic composition of Q (Figs. 5c–e; Wieler et al. 1992; Busemann et al. 2000). We also inferred that He and Ne were likely released from nanodiamonds or an unidentified phase with higher He/Ar and Ne/Ar ratios than phase Q proper (Fig. 9). The differences in the $^4He/^{36}Ar$ and $^{20}Ne/^{36}Ar$ ratios between gases released in the CSSE analyses of the Tagish Lake samples are mainly due to higher concentrations of He and Ne in the most altered sample 11v compared to the least altered sample 5b (Fig. S6). This is consistent with more gases being released from presolar nanodiamonds or an unidentified phase in 11v compared to 5b. Gilmour (2010) and Crowther and Gilmour (2013) showed that the heavy noble gases in the Q component could be a combination of fractionated solar gases with small and variable (0.2–3.3%) addition of HL gases known to reside in nanodiamonds. Similar to the conclusions in this study, Gilmour (2010) and Crowther and Gilmour (2013) suggested that the gases from the nanodiamonds could have been added to the Q component either during parent body alteration or during lab treatment.

Phase Q has not been isolated as an individual phase in spite of numerous attempts to do so (e.g., Verchovsky et al. 2002; Amari et al. 2013). It has been suggested that the Q-gases are trapped in the structure of IOM and that the Q-gases are released during oxidation due to rearrangement of the molecular structure of the IOM (Matsuda et al. 2010). Other authors favor a minor distinct carrier phase or phases of the Q-gases (e.g., Amari et al. 2013; Marrocchi et al. 2015). The differences in composition of "Q-gases" released in the samples in this study are best understood as differences in gas release from presolar grains. This data set, therefore, does not give much additional information about the carrier of the Q-gases. We conclude that in aqueously altered samples, primordial noble gas carriers other than phase Q proper have properties similar to those of phase Q, complicating the

determination of the noble gas composition in phase Q in aqueously altered samples. Samples that have experienced minimal aqueous and thermal alteration are best suited to determine the primordial composition of the noble gases in phase Q.

Implications for Q1 and Q2

Busemann et al. (2000) suggested that variations in $(^4He/^{36}Ar)_Q$ and $(^{20}Ne/^{36}Ar)_Q$ ratios between meteorites are due to the occurrence of two subtypes of Q: Q1 and Q2, and their distinct responses to alteration. This idea is illustrated with turquoise markings in Fig. 9. It was suggested that Q1 is more enriched in the light noble gases than Q2 and is released during mild etching, whereas Q2 contains less of the light noble gases and is released during more severe etching than Q1. This was based on the observation that the gases in the first etch steps during CSSE analyses of IOM with HNO_3 tend to have higher $^4He/^{36}Ar$ and $^{20}Ne/^{36}Ar$ ratios than later steps. The same pattern is observed in our data, with the exception of the very last etch steps, the composition of which probably reflect gas release from another carrier, see the Nanodiamonds section, Fig. 6. Busemann et al. (2000) observed that thermal metamorphism resulted in a decrease in the $^4He/^{36}Ar$ and $^{20}Ne/^{36}Ar$ ratios in Q, while the most aqueously altered samples have the highest $^4He/^{36}Ar$ and $^{20}Ne/^{36}Ar$ ratios (Fig. 9). To explain this observation, it was suggested that all samples initially incorporated Q-gases with roughly equal elemental ratios, similar to those of CM and CV chondrites and that parent body processing resulted in the variation seen in the ratios today (Busemann et al. 2000). In this model, subcomponent Q1 with higher $^4He/^{36}Ar$ and $^{20}Ne/^{36}Ar$ ratios than Q2 is less susceptible to aqueous alteration than to thermal metamorphism. The thermally metamorphosed samples would have lost Q1 gases, which lowered their $^4He/^{36}Ar$ and $^{20}Ne/^{36}Ar$ ratios. The aqueously altered samples would have retained their Q1 gases and maintained a more primitive Q composition with higher $^4He/^{36}Ar$ and $^{20}Ne/^{36}Ar$ ratios (Fig. 9).

The gases released from the more altered Tagish Lake sample 11v during CSSE had higher $^4He/^{36}Ar$ and $^{20}Ne/^{36}Ar$ ratios than those released from the less altered sample 5b (Fig. 9), in accordance with the observations of Busemann et al. (2000). However, our data are better explained by small amounts of noble gases being released from presolar grains in the most altered sample (see the Nanodiamonds section). To be in agreement with the Q1-Q2 model, our two samples should have released gases with roughly equal $^4He/^{36}Ar$ and $^{20}Ne/^{36}Ar$ ratios during CSSE analysis. They would have incorporated the same amounts of Q1 and Q2 and Q1 would not have been lost to a higher degree from 11v than 5b during aqueous alteration. We note that the more altered CM2 chondrite Cold Bokkeveld has higher $^4He/^{36}Ar$ and $^{20}Ne/^{36}Ar$ ratios in Q than the less altered CM2 chondrite Murchison (Fig. 9; Wieler et al. 1992; Busemann et al. 2000), consistent with the Tagish Lake data.

SUMMARY

Primordial noble gases in Tagish Lake are well explained by a mixture of the Q, HL, Ne-E, and P3 components. In addition, a component with high $^{20}Ne/^4He$ ratio compared to Q and HL is present, released during harsh etching in the CSSE analyses and in the 1200 °C heating step during pyrolysis. This component could originate from diamonds or perhaps from an unknown noble gas carrier. With the exception of Ne-E (carried by presolar SiC and graphite), there were only small variations in the concentrations of these components between the differently aqueously altered samples.

Ne-E(L) appears to have been lost from presolar graphite grains during aqueous alteration; concentrations of these gases decrease with increased alteration. In contrast, Ne-E(H) gases associated with presolar SiC are highest in the second most altered sample, 11i. To confirm that the Ne-E gases in 11i are from presolar SiC, we independently determined the abundance of SiC in the IOM samples by NanoSIMS mapping. The NanoSIMS data confirmed the noble gas results: the second most altered sample 11i was found to have an abundance of SiC grains about twice that of the other Tagish Lake samples. This heterogeneity in SiC abundance could be due to either heterogeneous accretion of the Tagish Lake parent body or redistribution of SiC on the parent body during alteration. Redistribution of SiC grains during aqueous alteration would require either significant fluid flow on the Tagish Lake parent body or perhaps a "mud ball convection" model for the Tagish Lake parent body (Bland and Travis 2017).

All of the SiC grains identified by the NanoSIMS measurements had $^{12}C/^{13}C$ ratios that are consistent with those of mainstream SiC grains originating from AGB stars. The average size of the grains was around 250–300 nm for all samples.

The data in this study highlight the problem with an operational definition of phase Q in which phase Q is a phase that survives IOM extraction and releases the Q-gases when IOM is treated with an oxidizing agent such as HNO_3 (Lewis et al. 1975). In the CSSE analyses, noble gases were extracted from IOM by etching with HNO_3, but in addition to Q-gases, noble gases associated with presolar grains were released.

Most visible were the Ne-E gases released from presolar SiC and graphite which obscured the Ne isotopic composition of Q. Presolar SiC grains were much more susceptible to oxidation in the more altered sample 11v than in the less altered sample 5b. Essentially the full budget of Ne-E was released in the 11v sample during etching with HNO_3, whereas only ~35% of the Ne-E in 5b was released. Hence, the concentration of Ne-E in oxidized residues cannot be used as a proxy for presolar SiC abundance in aqueously altered meteorites. In addition, He and Ne might have been released from presolar nanodiamonds or another unidentified phase during the CSSE analysis, affecting the elemental ratios. This has implications for the interpretation that Q1 and Q2 have different elemental ratios and react differently to alteration (cf. Busemann et al. 2000). The release of additional noble gases from presolar nanodiamonds during CSSE analysis is consistent with the interpretation of the Q-gases as being modified by small additions of HL gases from diamonds (Gilmour 2010; Crowther and Gilmour 2013). The best way to determine the uncontaminated, pristine composition of the Q-gases is probably through CSSE analysis of IOM from a sample with minimal aqueous alteration and thermal metamorphism.

We conclude that aqueous alteration can result in significant alteration to the behavior of some noble gas carriers, especially presolar SiC, and can lead to admixing of noble gases from presolar grains to the Q-gases, altering the perceived composition of Q. In addition, aqueous alteration can degas presolar graphite.

Acknowledgments—This article is dedicated to Christine Floss who was a remarkable scientist and left a big void in the cosmochemistry community when she passed away in spring 2018. The manuscript was greatly improved by reviews by Gary Huss, Jamie Gilmour, and associate editor Alex Ruzicka. Financial support was in part provided by the Swiss National Science Foundation through the National Center of Competence in Research PlanetS (HB, M.E.I.R) and grant P2EZP2_165234 (M.E.I.R).

Editorial Handling—Dr. Alexander Ruzicka

REFERENCES

Alexander C. M. O'D. 2005. Re-examining the role of chondrules in producing the elemental fractionations in chondrites. *Meteoritics & Planetary Science* 40:943–965.

Alexander C. M. O'D. 2019. Quantitative models for the elemental and isotopic fractionations in chondrites: The carbonaceous chondrites. *Geochimica et Cosmochimica Acta* 254:277–309.

Alexander C. M. O'D., Fogel M., Yabuta H., and Cody G. D. 2007. The origin and evolution of chondrites recorded in the elemental and isotopic compositions of their macromolecular organic matter. *Geochimica et Cosmochimica Acta* 71:4380–4403.

Alexander C. M. O'D., Cody G. D., Kebukawa Y., Bowden R., Fogel M. L., Kilcoyne A. L. D., Nittler L. R., and Herd C. D. K. 2014. Elemental, isotopic, and structural changes in Tagish Lake insoluble organic matter produced by parent body processes. *Meteoritics & Planetary Science* 49:503–525.

Amari S., Matsuda J.-I., Stroud M., and Matthew F. 2013. Highly concentrated nebular noble gases in porous nanocarbon separates from the Saratov (L4) meteorite. *The Astrophysical Journal* 778:37.

Basford J. R., Dragon J. C., Pepin R. O., and Coscio M. R. Jr 1973. Krypton and xenon in lunar fines. Proceedings, 4th Lunar Science Conference. pp. 1915–1955.

Bland P. A. and Travis B. J. 2017. Giant convecting mud balls of the early solar system. *Science Advances* 3: e1602514.

Bland P. A., Jackson M. D., Coker R. F., Cohen B. A., Webber J. B. W., Lee M. R., Duffy C. M., Chater R. J., Ardakani M. G., McPhail D. S., McComb D. W., and Benedix G. K. 2009. Why aqueous alteration in asteroids was isochemical: High porosity≠high permeability. *Earth and Planetary Science Letters* 287:559–568.

Blinova A. I., Zega T. J., Herd C. D. K., and Stroud R. M. 2014a. Testing variations within the Tagish Lake meteorite-I: Mineralogy and petrology of pristine samples. *Meteoritics & Planetary Science* 49:473–502.

Blinova A. I., Herd C. D. K., and Duke M. J. M. 2014b. Testing variations within the Tagish Lake meteorite-II: Whole-rock geochemistry of pristine samples. *Meteoritics & Planetary Science* 49:1100–1118.

Brearley A. J. 2006. The action of water. In *Meteorites and the early solar system II*, edited by Lauretta D. and McSween H. Y. Tucson, Arizona: The University of Arizona Press. pp. 587–624.

Brearley A. J. 2014. Nebular versus parent body processing. In *Treatise on geochemistry*, 2nd ed., edited by Holland H. D. and Turekian K. K. Oxford: Elsevier Science. pp. 309–334.

Brown P. G., Hildebrand A. R., Zolensky M. E., Grady M., Clayton R. N., Mayeda T. K., Tagliaferri E., Spalding R., MacRae N. D., Hoffman E. L., Mittlefehldt D. W., Wacker J. F., Bird J. A., Campbell M. D., Carpenter R., Gingerich H., Glatiotis M., Greiner E., Mazur M. J., McCausland P. J. A., Plotkin H., and Mazur T. R. 2000. The fall, recovery, orbit, and composition of the Tagish Lake meteorite: A new type of carbonaceous chondrite. *Science* 290:320–325.

Browning L. B., McSween H. Y., and Zolensky M. E. 1996. Correlated alteration effects in CM carbonaceous chondrites. *Geochimica et Cosmochimica Acta* 60:2621–2633.

Bullock E. S., Grady M. M., Russell S. S., and Gounelle M. 2005. Fe-Ni sulphides within a CM1 clast in Tagish Lake (abstract #1883). 36th Lunar and Planetary Science Conference. CD-ROM.

Busemann H. and Eugster O. 2002. The trapped noble gas component in achondrites. *Meteoritics & Planetary Science* 37:1865–1891.

Busemann H., Baur H., and Wieler R. 2000. Primordial noble gases in "phase Q" in carbonaceous and ordinary

chondrites studied by closed-system stepped etching. *Meteoritics & Planetary Science* 35:949–973.

Busemann H., Alexander C. M. O'D., Nittler L. R., and Wieler R. 2008. Noble gases in insoluble organic matter in the very primitive meteorites Bells, EET 92042 and GRO95577 (abstract #1777). 39th Lunar and Planetary Science Conference. CD-ROM.

Crowther S. A. and Gilmour J. D. 2013. The Genesis solar xenon composition and its relationship to planetary xenon signatures. *Geochimica et Cosmochimica Acta* 123:17–34.

Davidson J., Busemann H., Nittler L. R., Alexander C. M. O'D., Orthous-Daunay F.-R., Franchi I. A., and Hoppe P. 2014. Abundances of presolar silicon carbide grains in primitive meteorites determined by NanoSIMS. *Geochimica et Cosmochimica Acta* 139:248–266.

Davis A. M. and McKeegan K. D. 2014. Short-lived radionuclides and early solar system chronology. In *Treatise on geochemistry*, 2nd ed., edited by Holland H. D. and Turekian K. K. Oxford: Elsevier Science. pp. 361–395.

Eberhardt P., Jungck M. H. A., Meier F. O., and Niederer F. R. 1981. A neon-E rich phase in Orgueil: Results obtained on density separates. *Geochimica et Cosmochimica Acta* 45:1515–1528.

Gilmour J. D. 2010. "Planetary" noble gas components and the nucleosynthetic history of solar system material. *Geochimica et Cosmochimica Acta* 74:380–393.

Gilmour C. M., Herd C. D. K., and Beck P. 2019. Water abundance in the Tagish Lake meteorite from TGA and IR spectroscopy: Evaluation of aqueous alteration. *Meteoritics & Planetary Science*. https://doi.org/10.1111/maps.13362.

Göbel R., Ott U., and Begemann F. 1978. On trapped noble gases in ureilites. *Journal of Geophysical Research* 83:855–867.

Herd C. D. K., Blinova A., Simkus D. N., Huang Y., Tarozo R., Alexander C. M. O'D., Gyngard F., Nittler L. R., Cody G. D., Fogel M. L., Kebukawa Y., Kilcoyne A. L., Hilts R. W., Slater G. F., Glavin D. P., Dworkin J. P., Callahan M. P., Elsila J. E., De Gregorio B. T., and Stroud R. M. 2011. Origin and evolution of prebiotic organic matter as inferred from the Tagish Lake meteorite. *Science* 332:1304–1307.

Herd C. D. K., Sharp Z. D., Alexander C. M. O'D., and Blinova A. 2012. Oxygen isotopic composition of Tagish Lake lithologies: Insights into parent body alteration (abstract #1688). 43rd Lunar and Planetary Science Conference. CD-ROM.

Huss G. R. and Lewis R. S. 1994. Noble gases in presolar diamonds I: Three distinct components and their implications for diamond origins. *Meteoritics* 29:791–810.

Huss G. R. and Lewis R. S. 1995. Presolar diamond, SiC, and graphite in primitive chondrites—Abundances as a function of meteorite class and petrologic type. *Geochimica et Cosmochimica Acta* 59:115–160.

Huss G. R., Lewis R. S., and Hemkin S. 1996. The "normal planetary" noble gas component in primitive chondrites: Compositions, carrier, and metamorphic history. *Geochimica et Cosmochimica Acta* 60:3311–3340.

Huss G. R., Meshik A. P., Smith J. B., and Hohenberg C. M. 2003. Presolar diamond, silicon carbide, and graphite in carbonaceous chondrites: Implications for thermal processing in the solar nebula. *Geochimica et Cosmochimica Acta* 67:4823–4848.

Huss G. R., Rubin A. E., and Grossman J. N. 2006. Thermal metamorphism in chondrites. In *Meteorites and the early solar system II*, edited by Lauretta D. and McSween H. Y. Tucson, Arizona: The University of Arizona Press. pp. 567–586.

Keil K. 2000. Thermal alteration of asteroids: Evidence from meteorites. *Planetary and Space Science* 48:887–903.

Keil K., Zucolotto M. E., Krot A. N., Doyle P. M., Telus M., Krot T. V., Greenwood R. C., Franchi I. A., Wasson J. T., Welten K. C., Caffee M. W., Sears D. W. G., Riebe M., Wieler R., dos Santos E., Scorzelli R. B., Gattacceca J., Lagroix F., Laubenstein M., Mendes J. C., Schmitt-Kopplin P., Harir M., and Moutinho A. L. R. 2015. The Vicencia meteorite fall: A new unshocked (S1) weakly metamorphosed (3.2) LL chondrite. *Meteoritics & Planetary Science* 50:1089–1111.

Lambert D. L., Gustafsson B., Eriksson K., and Hinkle K. H. 1986. The chemical composition of carbon stars. I. Carbon, nitrogen, and oxygen in 30 cool carbon stars in the galactic disk. *The Astrophysical Journal Supplement Series* 62:373–425.

Lewis R. S., Srinivasan B., and Anders E. 1975. Host phase of a strange xenon component in Allende. *Science* 190:1251–1262.

Lewis R. S., Amari S., and Anders E. 1994. Interstellar grains in meteorites II: SiC and its noble gases. *Geochimica et Cosmochimica Acta* 58:471–494.

Marrocchi Y., Gounelle M., Blanchard I., Caste F., and Kearsley A. T. 2014. The Paris CM chondrite: Secondary minerals and asteroidal processing. *Meteoritics & Planetary Science* 49:1232–1249.

Marrocchi Y., Avice G., and Estrade N. 2015. Multiple carriers of Q noble gases in primitive meteorites. *Geophysical Research Letters* 42:2093–2099.

Matsuda J.-I., Lewis R. S., Takahashi H., and Anders E. 1980. Isotopic anomalies of noble gases in meteorites and their origins-VII. C3V carbonaceous chondrites. *Geochimica et Cosmochimica Acta* 44:1861–1874.

Matsuda J.-I., Morishita K., Tsukamoto H., Miyakawa C., Nara M., Amari S., Uchiyama T., and Takeda S. 2010. An attempt to characterize phase Q: Noble gas, Raman spectroscopy and transmission electron microscopy in residues prepared from the Allende meteorite. *Geochimica et Cosmochimica Acta* 74:5398–5409.

Moniot R. K. 1980. Noble-gas-rich separates from ordinary chondrites. *Geochimica et Cosmochimica Acta* 44:253–271.

Nakamura T., Noguchi T., Zolensky M. E., and Tanaka M. 2003. Mineralogy and noble gas signatures of the carbonate-rich lithology of the Tagish Lake carbonaceous chondrite: Evidence for an accretionary breccia. *Earth and Planetary Science Letters* 207:83–101.

Nittler L. R., Alexander C. M. O'D., Davidson J., Riebe M. E. I., Stroud R. M., and Wang J. 2018. High abundances of presolar grains and ^{15}N-rich organic matter in CO3.0 chondrite Dominion Range 08006. *Geochimica et Cosmochimica Acta* 226:107–131.

Ott U. 2014. Planetary and pre-solar noble gases in meteorites. *Chemie der Erde* 74:519–544.

Palguta J., Schubert G., and Travis B. J. 2010. Fluid flow and chemical alteration in carbonaceous chondrite parent bodies. *Earth and Planetary Science Letters* 296:235–243.

Quirico E., Bonal L., Beck P., Alexander C. M. O'D., Yabuta H., Nakamura T., Nakato A., Flandinet L., Montagnac G., Schmitt-Kopplin P., and Herd C. D. K. 2018.

Prevalence and nature of heating processes in CM and C2-ungrouped chondrites as revealed by insoluble organic matter. *Geochimica et Cosmochimica Acta* 241:17–37.

Rai V. K., Murty S. V. S., and Ott U. 2003. Noble gases in ureilites: Cosmogenic, radiogenic, and trapped components. *Geochimica et Cosmochimica Acta* 67:4435–4456.

Riebe M., Busemann H., Huber L., and Wieler R. 2013. Primordial noble gases in the unequilibrated LL3.2 chondrite Krymka analyzed by closed system step etching (abstract #2133). 44th Lunar and Planetary Science Conference. CD-ROM.

Riebe M. E. I., Busemann H., Wieler R., and Maden C. 2017a. Closed system step etching of CI chondrite Ivuna reveals primordial noble gases in the HF-solubles. *Geochimica et Cosmochimica Acta* 205:65–83.

Riebe M. E. I., Welten K. C., Meier M. M. M., Wieler R., Barth M. I. F., Ward D., Laubenstein M., Bischoff A., Caffee M. W., Nishiizumi K., and Busemann H. 2017b. Cosmic-ray exposure ages of six chondritic Almahata Sitta fragments. *Meteoritics & Planetary Science* 52:2352–2374.

Schelhaas N., Ott U., and Begemann F. 1990. Trapped noble gases in unequilibrated ordinary chondrites. *Geochimica et Cosmochimica Acta* 54:2869–2882.

Verchovsky A. B., Sephton M. A., Wright I. P., and Pillinger C. T. 2002. Separation of planetary noble gas carrier from bulk carbon in enstatite chondrites during stepped combustion. *Earth and Planetary Science Letters* 199:243–255.

Weigel A., Eugster O., Koeberl C., and Krahenbuhl U. 1997. Differentiated achondrites Asuka 881371, an angrite, and Divnoe: Noble gases, ages, chemical composition, and relation to other meteorites. *Geochimica et Cosmochimica Acta* 61:239–248.

Weimer D., Busemann H., Alexander C. M. O'D., and Maden C. 2017. The effect of aqueous alteration on primordial noble gases in CM chondrites (abstract #6300). 80th Annual Meeting of the Meteoritical Society.

Wieler R., Anders E., Baur H., Lewis R. S., and Signer P. 1991. Noble-gases in phase-Q—Closed system step etching of an Allende residue. *Geochimica et Cosmochimica Acta* 55:1709–1722.

Wieler R., Anders E., Baur H., Lewis R. S., and Signer P. 1992. Characterization of the Q-gases and other noble gas components in the Murchison meteorite. *Geochimica et Cosmochimica Acta* 56:2907–2921.

Young E. D., Ash R. D., England P., and Rumble D. III 1999. Fluid flow in chondritic parent bodies: Deciphering the compositions of planetesimals. *Science* 286:1331–1335.

Zinner E. 2014. Presolar grains. In *Treatise on geochemistry*, 2nd ed., edited by Holland H. D. and Turekian K. K. Oxford: Elsevier Science. pp. 181–213.

Zolensky M. E., Nakamura K., Gounelle M., Mikouchi T., Kasama T., Tachikawa O., and Tonui E. 2002. Mineralogy of Tagish Lake: An ungrouped type 2 carbonaceous chondrite. *Meteoritics & Planetary Science* 37:737–761.

SUPPORTING INFORMATION

Additional supporting information may be found in the online version of this article.

Fig. S1. Carbon isotopic compositions of presolar SiC grains.

Fig. S2. Examples of NanoSIMS areas defined as and not defined as a SiC grain.

Fig. S3. Xe isotopic compositions of the gases released in the CSSE experiments and during stepwise heating of the oxidized IOM.

Fig. S4. Concentrations in cm^3STP/g IOM of major noble gas isotopes in the un-oxidized IOM.

Fig. S5. Histogram showing the diameters of individual presolar SiC grains.

Fig. S6. Comparison of the concentrations of major isotopes (^4He, ^{20}Ne, ^{36}Ar, ^{84}Kr, ^{132}Xe) between 11v and 5b in the different analyses.

Fig. S7. Cumulative release pattern of major isotopes in the two CSSE experiments.

Table S1. Kr isotopic compositions of individual etch steps in CSSE analyses of 5b and 11v.

Table S2. He and Ar isotopic compositions of individual etch steps in CSSE analyses of 5b and 11v.

Table S3. Xe isotopic composition of individual etch steps of CSSE analysis of 5b.

Table S4. Xe isotopic compositions of individual etch steps of CSSE analysis of 11v.

Table S5. Isotopic compositions of He, Ar, and Kr in individual temperature steps during stepwise pyrolysis.

Table S6. Isotopic compositions of Xe in individual temperature steps during stepwise pyrolysis.

Data S1. Component deconvolution.